WRF-Chem simulations of CO₂ over Belgium and surrounding countries assessed by ground-based measurements

Jiaxin Wang[1,2,3,4], Sieglinde Callewaert[4], Minqiang Zhou[1], Filip Desmet[4], Sébastien Conil[5], Michel Ramonet[6], Pucai Wang[2,3], Martine De Mazière[4]

[1]State Key Laboratory of Atmospheric Environment end Extreme Meteorology, Institute of Atmospheric Physics, Chinese Academy of Sciences, Beijing 100029, China
[2]LAGEO, Institute of Atmospheric Physics, Chinese Academy of Sciences, Beijing 100029, China
[3]University of Chinese Academy of Sciences, Beijing 100049, China
[4]Royal Belgian Institute for Space Aeronomy (BIRA-IASB), Brussels 1180, Belgium
[5]ANDRA DISTEC/EES Observatoire Pérenne de l'Environnement, F-55290, Bure, France
[6]Laboratoire des Sciences du Climat et de l'Environnement, LSCE-IPSL (CEA-CNRS-UVSQ), Université Paris-Saclay 91191 Gif-sur-Yvette, France

Correspondence to: Sieglinde Callewaert (sieglinde.callewaert@aeronomie.be) and Minqiang Zhou (minqiang.zhou@mail.iap.ac.cn)

Abstract. The Weather Research and Forecasting model coupled with Chemistry (WRF-Chem), in its passive tracer option (WRF-GHG), was used to simulate CO_2 concentrations over Western Europe during summer 2018. The model performance was evaluated against ground-based observations. Due to the large variety of anthropogenic emissions, we conducted five sensitivity tests using a combination of three different inventories (CAMS-REG-ANT, EDGAR, and TNO) and source-specific vertical emission profiles. Compared with observations from five Integrated Carbon Observation System (ICOS) atmospheric stations, the model captures diurnal CO_2 variations at different heights. At the ICOS site in Karlsruhe, Germany, simulated near-surface CO_2 mole fractions are highly sensitive to the choice of ~~anthropogenic emission~~ inventory, with discrepancies up to 14.99±31.98 ppm, due to large nearby emission sources. Furthermore, incorporating source-specific vertical profiles notably improves accuracy, increasing the correlation coefficient from 0.53 to 0.78 when using EDGAR. The column-averaged dry-air mole fractions of CO_2 (XCO_2) from the Total Column Carbon Observing Network (TCCON) are well simulated by WRF-GHG. However, an overestimation of approximately 1.2 ppm was found at the Paris site, likely due to uncertainties in background fields and anthropogenic emissions. In addition, a negative bias was found in early June at most ICOS and TCCON sites, may be attributed to errors in simulated fluxes during the growing season. However, due to the lack of co-located flux observations, the exact cause remains uncertain. Overall, this study demonstrates the capability of WRF-GHG in simulating CO_2 over Belgium and surrounding countries and provides insights into the regional-scale characteristics of atmospheric CO_2 ~~while showing the need for improving model configuration~~.

1 Introduction

Intergovernmental Panel on Climate Change Sixth Assessment Report (IPCC AR6) points out that human-induced climate change has significantly influenced the frequency and intensity of extreme events such as heatwaves, heavy precipitation, droughts, and tropical cyclones (Pörtner et al., 2022). In recent years, extreme heat events have become increasingly frequent in western Europe, with prolonged durations of heatwaves (Della-Marta et al., 2007; Sousa et al., 2020; Sánchez-Benítez et al., 2022). The Paris Agreement proposes to limit the global temperature increase to within 2°C above pre-industrial levels. To achieve this long-term goal, governments must implement measures to reduce carbon emissions. The atmospheric mole fractions of carbon dioxide (CO_2), a major greenhouse gas (GHG), have steadily risen due to human activities over the last centuries. By March 2025, the global mean mole fractions of CO_2 had increased to 426.40 ppm (Lan et al., 2025). Accurate estimation of carbon emissions is a crucial prerequisite for formulating scientifically sound and effective emission reduction strategies.

The 2019 refinement of the 2006 IPCC Guidelines for National Greenhouse Gas Inventories (Maksyutov et al., 2019) explicitly states that the top-down method, based on atmospheric inverse modelling, can serve as a potential way to support and verify national greenhouse gas inventories. However, several studies identified uncertainties associated with atmospheric transport models as one of the main sources of error in this approach (Díaz Isaac et al., 2014; Feng et al., 2016). Therefore, reducing transport errors and improving simulation accuracy are essential for improving the reliability of inversion results.

Regional atmospheric transport models have been widely applied to simulate CO_2 mole fractions, mainly focusing on national or urban scale (Zhao et al., 2019; Zhao et al., 2023; Thilakan et al., 2024; Yang et al., 2025), but their simulation results still present some drawbacks and limitations. Previous studies have shown that the quality of model simulations is highly dependent on the boundary conditions and emission inventories accuracy (Callewaert et al., 2022; Karbasi et al., 2025). Additionally, Brunner et al. (2019) pointed out that using CO_2 emissions only at the surface causes a significant overestimation of the simulated near-surface CO_2 mole fractions, highlighting the need for properly allocating the vertical signature of emissions.

In order to support accurate assessments of greenhouse gas budgets, various ground-based observation networks have been established to provide consistent and high-precision data, such as Integrated Carbon Observation System (ICOS) Atmosphere in Europe. In situ observations provide near-surface CO_2 mole fractions data, which can be used to constrain carbon sources and sinks at local scales. Using the ICOS atmospheric measurements, Ramonet et al. (2020) reported that a severe drought event in Europe in 2018 led to an atmospheric CO_2 signal of +1 to +2 ppm at most stations in summer. Ground-based remote sensing observations, on the other hand, offer information on total column abundances. The global Total Carbon Column Observing Network (TCCON, Wunch et al., 2011) provides long-term, high-precision column-averaged mole fraction measurements that commonly serve as validation data for satellite remote sensing observations (Velazco et al., 2019; Yang et al., 2020; Zhou et al., 2022) and for model verification (Saito et al., 2012; Turner et al., 2015; Ostler et al., 2016). A signal of 0.8 ppm was observed at the Sodankylä TCCON site during the 2018 drought (Ramonet et al., 2020). Since the magnitude of these signals is less than 2 ppm, it is still difficult for satellites to detect such variations (Connor et al., 2016).

Belgium is located in the central part of Western Europe, serving as an important hub connecting France, Germany, the Netherlands, and Luxembourg, and positioned at the intersection of continental transportation. To support climate change mitigation commitments and policy development, the project Towards a greenhouse gas emission monitoring and VERification system for BElgium (VERBE), led by the Royal Belgian Institute for Space Aeronomy (BIRA-IASB), proposes to establish an independent, top-down, temporally and spatially resolved Monitoring and Verification Support (MVS) capacity for greenhouse gas (GHG) emissions in Belgium. To our knowledge, there are no ground-based CO_2 observations, and there aren't any CO_2 model-based studies specifically for the Belgium region currently, while a few studies have been conducted in neighbouring Western European countries (Lian et al., 2021; van der Woude et al., 2023; Zhao et al., 2023).

The study presented in this paper has been performed in the framework of the VERBE project. It employs the Weather Research and Forecasting Greenhouse Gas model (WRF-GHG; Beck et al., 2011) and multi-source observational data to simulate and evaluate CO_2 mole fractions over Western Europe, with a focus on Belgium and surrounding regions during summer 2018. The aim is to evaluate the model performance in this region and analyse the spatial and temporal variations of CO_2 mole fractions. Different sensitivity tests were used to investigate the impact of different anthropogenic emission inventories on the model simulations performance and to optimize the WRF-GHG configuration, in order to improve the regional greenhouse gas simulation accuracy and carbon budget inversion in the near future.

This paper is structured as follows: the introduction to the WRF-GHG model setup and input datasets is given in Sect. 2. The observational datasets and the statistical metrics used to evaluate the model performance are described in Sect. 3. The evaluation of the simulation results, focusing on meteorological fields and CO_2 concentration fields are presented in Sect. 4. The simulation errors looking especially at anthropogenic emissions and biogenic sources are discussed in Sect. 5. Finally, the conclusions are drawn in Sect. 6.

2 WRF-GHG model

The passive tracer option in the WRF model coupled with Chemistry (WRF-Chem), also known as WRF-GHG, can be used to simulate the spatiotemporal distribution of long-lived GHGs like CO_2 and CH_4. In this configuration, the long-lived gases are transported in a passive way without any chemical reactions (Beck et al., 2011). Here WRF-Chem model version 4.5.1 was used.
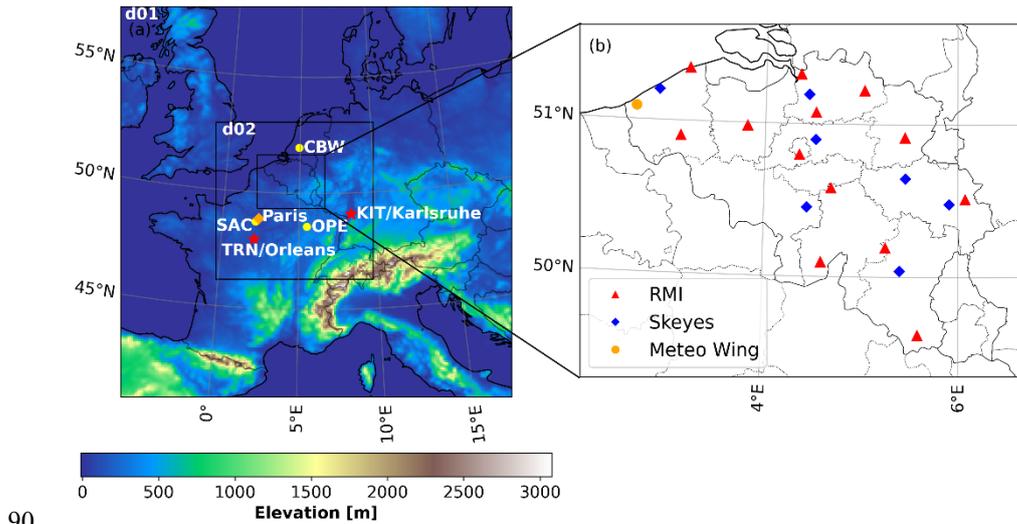
2.1 Model settings

Figure 1. Terrain elevation map of the simulated domains, with horizontal resolutions of 9 km (d01) and 3 km (d02), showing ICOS (yellow dots), TCCON (orange diamond) and co-located (red stars) sites within d02 (a), and synoptic stations in Belgium for which data are available for our study period (b).

The simulation area covers Western Europe and is centered on Belgium. As shown in Fig. 1(a) using the Lambert Conformal Conic (LCC) projection, two nested domains are configured, with horizontal resolutions of 9 km for the outer domain and 3 km for the inner domain. The vertical grid consists of 60 sigma levels extending from the surface up to 50 hPa. Due to the similarity of the simulation domains, the physical parameterization settings were the same as the settings of Poraicu et al. (2023), except for the urban surface. The Multi-layer Building Effect Parameterization (BEP) model (Martilli et al., 2002) was used instead of the Single-layer Urban Canopy Model (UCM) (Kusaka et al., 2001) because the latter is incompatible with the GHG option. For the Planetary Boundary Layer, we have chosen the Yonsei University scheme (YSU) (Hong et al., 2006).

In the summer of 2018, Europe experienced an intense and widespread heatwave that had a significant impact on ecosystem processes (Bastos et al., 2020; Thompson et al., 2020; Smith et al., 2020). According to records from the Royal Meteorological Institute of Belgium (RMI) at the Uccle station, the total precipitation for the summer (June to August) of 2018 was 134.7 mm, which was substantially lower than the climatological mean for the summer period 1991-2020 (234.2 mm). Meanwhile, this period occurred before the outbreak of the COVID-19 pandemic, during which the ground-based observation network operated normally and provided abundant observational data, laying a solid foundation for model validation and analysis. Therefore, our simulation period covers the summer from 1st June to 31st August 2018. In this study, the meteorological fields are re-initialized every 24 hours, with a 6-hour spin-up applied before each re-initialization. By doing this, we can constrain the meteorological fields. This approach has been applied in many studies and has proven to improve the simulations accuracy (Pillai et al., 2011; Zhao et al., 2019; Ho et al., 2024).

4

2.2 Input dataset

In WRF-GHG, the simulated CO_2 ($CO_{2,total}$) is the sum of several tracer contributions distinguishing different sources and sinks that are driven by specific emission inventories or flux models, and the so-called background concentrations that are driven by the initial and boundary conditions. Thus, the simulated CO_2 concentrations are given by:

115
$$CO_{2,total} = CO_{2,bck} + CO_{2,ant} + CO_{2,bio} + CO_{2,bbu} + CO_{2,oce} \,, \tag{1}$$

where $CO_{2,bck}$ represents the background concentration, and the remaining terms represent contributions from anthropogenic emissions ($CO_{2,ant}$), biogenic activities ($CO_{2,bio}$), biomass burning emissions ($CO_{2,bbu}$), and ocean-atmosphere exchange ($CO_{2,oce}$), respectively. Table 1 gives an overview of the input datasets employed in the simulation, apart from anthropogenic emissions, along with their temporal and spatial resolutions. For initial and lateral boundary conditions, the meteorological

120 fields are provided by the European Centre for Medium-Range Weather Forecasts (ECMWF) global ERA5 hourly reanalysis dataset on model levels, which includes 137 vertical levels (Hersbach et al., 2020), and the chemical fields are provided by the 3-hourly Copernicus Atmosphere Monitoring Service (CAMS) global greenhouse gas reanalysis (EGG4) which includes 60 vertical model levels (Inness et al., 2019). For the emissions, the open biomass burning flux is obtained from the daily Fire INventory from NCAR (FINN v2.5; Wiedinmyer et al., 2023), and the CO_2 fluxes from the oceans are taken from the

125 observation-based global monthly gridded sea surface pCO_2 climatology (NCEI; Landschützer et al., 2019). Given the significant influence of anthropogenic activities throughout much of the study area, the choice of anthropogenic emission inventory can greatly affect the simulation accuracy. The sensitivity tests using different inventories and setups will be discussed later (see Sect. 2.3).

Table 1. Overview of input datasets, excluding anthropogenic emissions.

	Components	Source	Resolution	
			Temporal	Spatial
Initial and lateral boundary conditions	Meteorological	ERA5 reanalysis	1h	0.25°×0.25°
	Chemical	CAMS global reanalysis for greenhouse gas	3h	0.75°×0.75°
Fluxes	Biogenic	Online (VPRM)	Daily	Model resolution
	Biomass burning	Fire INventory from NCAR (FINN) v2.5	Daily	1km
	Ocean	Observation-based global monthly gridded sea surface pCO_2 fields	Monthly	1°×1°

130

Biogenic CO_2 flux from the vegetation also plays a significant role during the summer. Here, we use the Vegetation Photosynthesis and Respiration Model (VPRM) (Mahadevan et al., 2008), which is coupled online with WRF-GHG. In VPRM, the calculation of net ecosystem exchange (NEE) consists of two components: gross primary production (GPP) and respiration (R_{res}). Since vegetation photosynthesis acts as a sink for CO_2, GPP is represented as a negative flux in the WRF-GHG model

135 calculations.
$$NEE = GPP + R_{res} \,, \tag{2}$$

$$GPP = -\lambda T_{scale} \cdot W_{scale} \cdot P_{scale} \cdot EVI \cdot \frac{PAR}{1+\frac{PAR}{PAR_0}} , \qquad (3)$$

$$R_{res} = \alpha T_s + \beta . \qquad (4)$$

Here, Photosynthetically Active Radiation (PAR) is assumed to be approximately equal to the downward shortwave radiation
140 (SW) in the WRF-GHG model (i.e., $PAR \approx SW$). The 2m temperature (T_s) and PAR are provided by WRF simulations. T_{scale} represents the temperature sensitivity of photosynthesis, which is defined by a minimum, maximum and optimum temperature ($T_{min}, T_{max}, T_{opt}$) for photosynthesis for each vegetation class (Evergreen Forest, Deciduous Forest, Mixed Forest, Shrubland, Wetland, Cropland, Grassland and Other.). $\lambda, PAR_0, \alpha, \beta$ are four parameters that depend on the vegetation class. Considering their importance, and following sensitivity tests (not shown here), these parameters (see Table A1) are adopted
145 from Table 3 in the preprint of Glauch et al. (2025). Notably, in Glauch et al. (2025), they employ the formulation $PAR \approx 0.505 \times SW$, which differs from the default setting $PAR \approx SW$ in WRF-GHG used here. W_{scale} and P_{scale} represent the effect of water stress and leaf age on photosynthesis, respectively. They are both calculated using the Land Surface Water Index (LSWI) (Xiao et al., 2004). Here, the Enhanced Vegetation Index (EVI) and LSWI are derived from the surface reflectance values of 500-m-resolution Moderate Resolution Imaging Spectroradiometer (MODIS) (Huete et al., 2002; Gao.,
150 1996). The Copernicus Dynamic Land Cover Collection 3 (Buchhorn et al., 2020) with a high spatial resolution of 100 meters is used to calculate the fraction of each vegetation class in every continental grid cell. The VPRM Preprocessor class in pyVPRM was used to generate the input data needed in VPRM (Glauch, et al., 2025).

2.3 Anthropogenic emission settings

Considering the importance of anthropogenic emissions inventories and the availability of multiple options, we conducted a
155 sensitivity analysis of anthropogenic CO_2 emissions using five different input configurations, based on three different emission inventories, as summarized in Table 2. (1-2) Monthly sector-specific gridmaps of EDGAR v2024, with a spatial resolution of 0.1°×0.1° (Crippa et al ., 2024). (3-4) Yearly CAMS-REG-ANT v8.0 sector-specific gridmaps, with a spatial resolution of 0.1◦×0.05◦ (Kuenen et al., 2022). (5) Yearly TNO_GHGco_v4.1, with a spatial resolution of 1/60◦× 1/120◦ (∼ 1 × 1 km over central Europe) (Super et al., 2020). As the TNO inventory doesn't encompass the entire simulation domain, emissions in areas
160 outside its coverage are supplemented using the CAMS-REG-ANT inventory. Considering temporal variation, for EDGAR v2024, due to the lack of corresponding sector-specific temporal factors, we assumed constant hourly values within each month. For CAMS-REG-ANT and TNO, we downscaled the yearly fluxes to hourly emissions data, using the sector-specific factors from CAMS-REG-TEMPO (Guevara et al., 2021) and temporal profile factors from Nassar et al. (2013), respectively. In addition to comparing different emission inventories, we also evaluated the impact of accounting for the height of
165 anthropogenic emission point sources. As pointed out by Brunner et al. (2019), more than 50% of CO_2 emissions in Europe are emitted by large point sources, primarily released through stacks and cooling towers, underscoring the importance of accurately representing the vertical distribution of anthropogenic emissions in model simulations. Assuming all anthropogenic emissions are released from point sources, a vertical disaggregation was applied to the sector-specific emission inventories

from (2) EDGAR and (4) CAMS-REG-ANT, using the vertical emission profiles provided by Brunner et al. (2019).
Anthropogenic sources are classified into 10 different categories according to the Selected Nomenclature for Air Pollutants (SNAP) in the study by Brunner et al. (2019) on vertical profiles, and the sector mapping between different inventories is detailed in Table A2.

Table 2. Overview of the five different anthropogenic emissions inputs. The type "S" represents all emissions released at the surface. "P" represents anthropogenic emissions released according to source-specific vertical profiles (Brunner et al., 2019).

	Test	Type	Inventory	Resolution
1	EDGAR_S	S	EDGAR v2024 (sector-specific)	Monthly 0.1°×0.1°
2	EDGAR_P	P		
3	CAMS_S	S	CAMS-REG-ANT v8.0 (sector-specific)	Yearly 0.1°×0.05°
4	CAMS_P	P		
5	TNO_CAMS	S	TNO_GHGco_v4.1 + CAMS-REG-ANT v8.0	Yearly 1/60° × 1/120° (for TNO)

3 Observations and methods

We collected observational data for both meteorological and chemical fields, consisting of three types: meteorological observations, in-situ and ground-based remote sensing CO_2 observations. Unfortunately, CO_2 concentration measurements are lacking within Belgium during this period, therefore, we gathered observational data from the surrounding regions of Belgium.

3.1 Synoptic observations in Belgium

A meteorological observation network is operated across Belgium by the RMI, Meteorological Wing of the Air Component of Defense (Meteo Wing), and the Belgian Authority of airways that is the Belgian air navigation and traffic service provider for the civil airspace (Skeyes). To ensure data quality, the synoptic data provided by RMI undergo a quality control (QC) procedure consisting of an automatic process followed by manual supervision, whereas the QC of data from stations belonging to Skeyes and Meteo Wing is conducted independently of RMI (Bertrand et al., 2013). Figure. 1(b) shows the locations of the 21 stations from which observations are currently available, where red triangles represent 13 stations operated by RMI, blue diamonds represent 7 stations operated by Skeyes, and the orange dot represents 1 station operated by Meteo Wing. Their detailed coordinates are listed in Table A3. These sites are mainly situated on areas covered by short grass and provide hourly near-surface weather parameters, including temperature, wind speed and wind direction. To evaluate the WRF-GHG model performance, the simulated 2-meter temperature (T2) and 10-meter wind speed (WS10) and wind direction (WD10) from the grid nearest to each station within the inner domain were compared with the observations. It's worth noting that there are eight stations operated by Skeyes and Meteo Wing where wind speed and wind direction observations are recorded only as integer values.

3.2 ICOS – Atmospheric stations

The ICOS (ICOS RI, 2023) atmospheric observation network covers the European region and provides standardized, high-precision scientific data on the carbon cycle and greenhouse gas budgets. It currently comprises 46 stations in 16 countries and there are 5 sites located with available observational data within our inner domain, including Observatoire Pérenne de l'Environnement (OPE), Saclay (SAC), Cabauw (CBW), Trainou (TRN), and Karlsruhe (KIT). Their locations are shown in Fig. 1(a), with details on site coordinates and observation heights listed in Table 3. Each site is equipped with meteorological instruments and Picarro CRDS (Cavity Ring-Down Spectroscopy) GHG analyzers installed at multiple heights on tall towers, providing measurements of hourly meteorological parameters and in situ CO_2 mole fractions. For comparison with the simulation results, the simulation data from the inner domain nearest grid cell for each observation site are first extracted. Given that the observation heights at each site do not correspond directly to the model levels, the extracted model data are subsequently interpolated to the corresponding observation heights.

Table 3. The relevant information for each station. 'm a.s.l.' stands for meters above sea level, and 'm a.g.l.' stands for meters above ground level.

Station		Location	Altitude (m a.s.l.)	Observation Height (m a.g.l.)
Karlsruhe	KIT	49.0915°N 8.4249°E	110	30/60/100/200
Trainou	TRN	47.9647°N 2.1125°E	131	50/100/180
Saclay	SAC	48.7227°N 2.142°E	16	60/100
Observatoire Pérenne de l'Environnement	OPE	48.5619°N 5.5036°E	390	50/120
Cabauw	CBW	51.9703°N 4.9264°E	0	207

3.3 TCCON

TCCON is a global ground-based observation network of Fourier Transform Spectrometers (FTS). It uses the GGG software to retrieve gases mole fractions with high precision and is currently widely used for the validation of satellite measurements (Zhou et al, 2016; Karbasi et al, 2022; Wu et al, 2018). There are three observation sites, Orléans (47.97°N 2.11°E), Karlsruhe (49.10°N 8.44°E), and Paris (48.85°N 2.36°E), located within the inner domain. Among them, the Orléans and Karlsruhe sites are co-located with the ICOS TRN and KIT sites, respectively, and the Paris site is located in an urban area. Each site is equipped with a Bruker IFS 125HR instrument to record shortwave infrared (SWIR) spectra and use the GGG2020 code to retrieve the column-averaged dry air mole fractions of CO_2 (XCO_2) (Laughner et al., 2024). TCCON observations are limited to daytime and clear-sky only. To ensure a meaningful comparison with WRF-GHG outputs, the observational data within a 30-minute interval before and after the corresponding model time step are averaged. Additionally, a smoothing correction to account for the a priori profile and averaging kernels (AVKs) associated with the TCCON data was applied to the simulations

data before comparison (Rodgers and Connor, 2003). Details on this correction can be found in Appendix B1 of Callewaert et al. (2022).

3.4 Evaluation metrics

220   To evaluate the performance of the WRF-GHG model, we employed several statistical metrics. The mean bias error (MBE) quantifies the systematic bias between simulations and observations, the standard deviation (STD) of the simulation-observation differences reflects the variability of the simulations relative to the observations, the root mean square error (RMSE) of the difference quantifies the overall magnitude of simulation uncertainties, and the Pearson correlation coefficient (R) reflects the strength of the expected linear relationship between simulated and observed values. These metrics have been widely

225   used in the assessment of model simulations (e.g. Callewaert et al, 2023; Yarragunta et al, 2025). Their calculation formulas are as follows:

$$Diff_i = mod_i - obs_i , \tag{5}$$

$$MBE = \frac{\sum_{i=1}^{N} Diff_i}{N} , \tag{6}$$

$$STD = \sqrt{\frac{1}{N}\sum_{i=1}^{N}(Diff_i - MBE)^2} , \tag{7}$$

230   $$RMSE = \sqrt{\frac{1}{N}\sum_{i=1}^{N} Diff_i^2} , \tag{8}$$

$$R = \frac{\sum_{i=1}^{N}(mod_i - \overline{mod})(obs_i - \overline{obs})}{\sqrt{\sum_{i=1}^{N}(mod_i - \overline{mod})^2} \cdot \sqrt{\sum_{i=1}^{N}(obs_i - \overline{obs})^2}} , \tag{9}$$

where mod_i represents the WRF-GHG simulated values, obs_i represents the observed values, and N is the number of data pairs.

4 Model performance

4.1 Meteorological fields

235

The overall evaluation metrics between simulated and observed near-surface temperature, wind speed, and wind direction across all 21 synoptic observation stations in Belgium are given in Table 4, and N represents the number of data pairs. The detailed values at each station can be found in Table A3, and the map is shown in Fig. A1. As mentioned in Sect. 3.1, the wind direction and wind speed observations at eight stations are recorded only as integer values, which limits the ability to capture fine-scale variations and primarily reflect overall trends. Despite the lack of high-precision observations, the WRF model

240   reproduces these variation patterns reasonably well at the trend level. The near-surface temperature was well simulated by the model, with MBE of -0.07K and R as high as 0.95. Regarding wind fields, the observed wind speed and direction exhibit more pronounced fluctuations than the simulations, as also reported by Zhao et al. (2019). This may result from the rapid changes in real atmospheric conditions, which are difficult for models to capture. Besides, as shown in Fig. A1, the model tends to

underestimate wind speed values significantly along coastal regions, with an MBE of -1.11 m/s across the four coastal stations, which is probably due to the coastal effects in the WRF simulation (Hahmann et al., 2015). In inland areas, the model tends to overestimate at most sites with dense vegetation cover. Such overestimation of wind speed has also been found in previous studies (Duan et al., 2018; Liu et al., 2022; Che et al., 2024). This bias may be attributed to the complex wind distribution in areas with rugged terrain, where the WRF model fails to adequately account for the additional resistance effects of vegetation on unresolved terrain, ultimately leading to an overestimation of wind speed. While an underestimation of wind speed is also observed at some inland stations, most of these stations are located at airports or in areas dominated by cropland. The land-use classification of the corresponding model grid cells is mostly identified as urban and built-up, which may lead to an overestimation of the surface roughness near the station and consequently an underestimation of wind speed. Similar findings were reported by Aylas et al. (2020), who found that WRF underestimated wind speed at airport stations by approximately -0.124 m/s, while the bias was reduced to -0.079 m/s after updating the land-use data.

**Table 4. Evaluation metrics between simulated and observed temperature, wind speed, and wind direction across all 21 stations.**

	N	MBE	STD	RMSE	R
Temperature (K)	44405	-0.07	1.61	1.61	0.95
Wind Speed (m/s)	43822	-0.20	1.45	1.47	0.63
Wind Direction (°)	41967	3.31	43.16	43.29	0.57

In comparison with ICOS observations, there were no meteorological observations available at KIT and CBW stations, as well as at the 100 m height at TRN site during the simulation period. For the remaining sites, the diurnal cycles of temperature and wind speed, along with the time series of wind direction, are shown in Fig. 2. The values in each subplot represent the corresponding MBE ± STD values between the simulations and the observations. In the diurnal variation plots, the solid lines represent the mean values at the same time of day throughout the simulation period, while the shaded areas indicate the standard deviation. Similar to the RMI observation sites, the model simulates temperature well at different heights across all ICOS stations, with MBE of less than 0.22 K. As for wind speed, the model captures the diurnal variation at each site, showing higher wind speeds at night and lower speeds during the day. However, it tends to overestimate the wind speed values, especially as the height gets closer to the surface, such as at 50 m at TRN and OPE stations, and at 60 m at SAC station. This agrees with Tuccella et al. (2012), who pointed out that the model can capture the upper-level wind speed profile but tends to overestimate it in the lower layers. Besides the model tends to significantly overestimate wind speed during the night, as also shown in previous studies (Zhang and Zheng, 2004; Ngan et al., 2013; Dayal et al., 2020). These wind speed simulation errors may be due to limitations of some parameterization of physical processes during the daytime or nighttime, such as turbulence and surface roughness. Additionally, at the OPE and SAC stations, low-level jets (LLJs) frequently occur near the top of the nocturnal boundary layer (NBL), where excessive downward momentum transport may also lead to overestimated wind speeds (Zhang and Zheng, 2004). For wind direction, the model can simulate it well, except at the height of 50 m at OPE site. We additionally compared the wind direction observations at the 50 m height at the OPE site, obtained from an independent ICOS

instrument through personal communication with the Principal Investigator (PI), with the model simulation results (not shown). Compared to the ICOS data, this independent observation shows better agreement with the model. There might be uncertainties or measurement errors in the wind direction data from the ICOS anemometer at the 50 m height, which could stem from the sensor itself or be related to its setup, possibly affected by disturbances from the tower structure. The wind speed measurements at the 50m level at OPE are also most probably affected by these limitations.

Overall, the model captures the near-surface variations in meteorological fields well, and exhibits high accuracy in the vertical profiles, which are similar to the performances displayed in previous studies (Tuccella et al., 2012; Mar et al., 2016; Zhao et al., 2023).
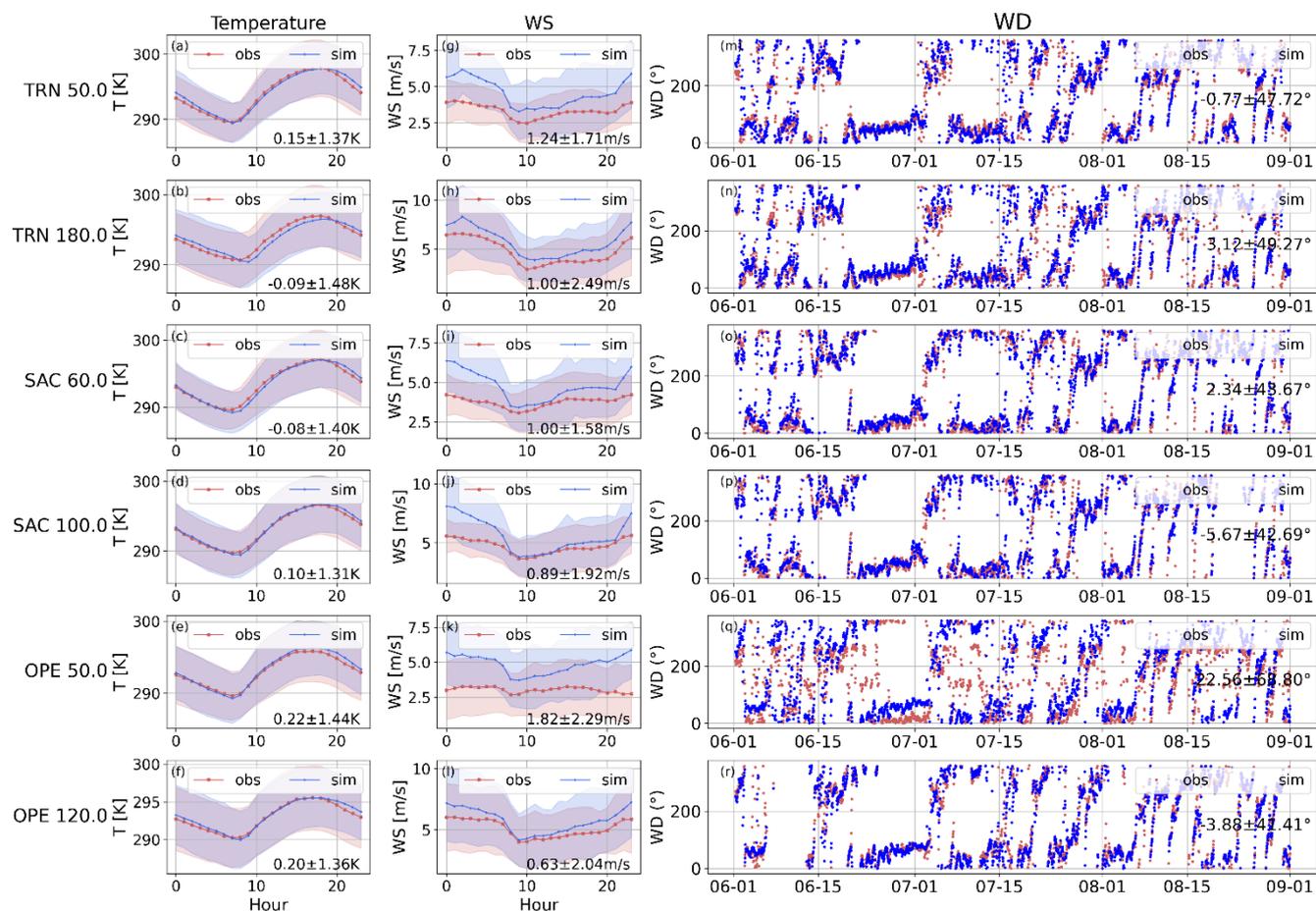
Figure 2. The diurnal cycles of temperature (a-f) and wind speed (g-l), and the time series of wind direction (m-r) at different heights at various ICOS stations. The time is local time (UTC+2).

4.2 Chemical fields

The simulated CO_2 mole fractions are compared with corresponding observations in this section.

11

4.2.1 Comparisons with ICOS – near surface CO₂ mole fractions

The statistical metrics for differences in near-surface CO_2 mole fractions between simulations using five different anthropogenic emission settings and observations at different heights above ground across various ICOS sites are given in Fig. 3. At most sites, the values of STD and RMSE between the simulations and observations tend to increase at lower heights. Additionally, when anthropogenic emissions are released only at the surface, the differences in simulation results between emission inventories can be significant. For example, using surface emission from either EDGAR or TNO can lead to differences up to 14.99 ± 31.98 ppm (MBE ± STD) at the KIT site at 30 m height. It reflects that the anthropogenic emission inventory has a significant impact on the simulation of near-surface CO_2 mole fractions, especially at lower heights above ground-level and for peri-urban stations.
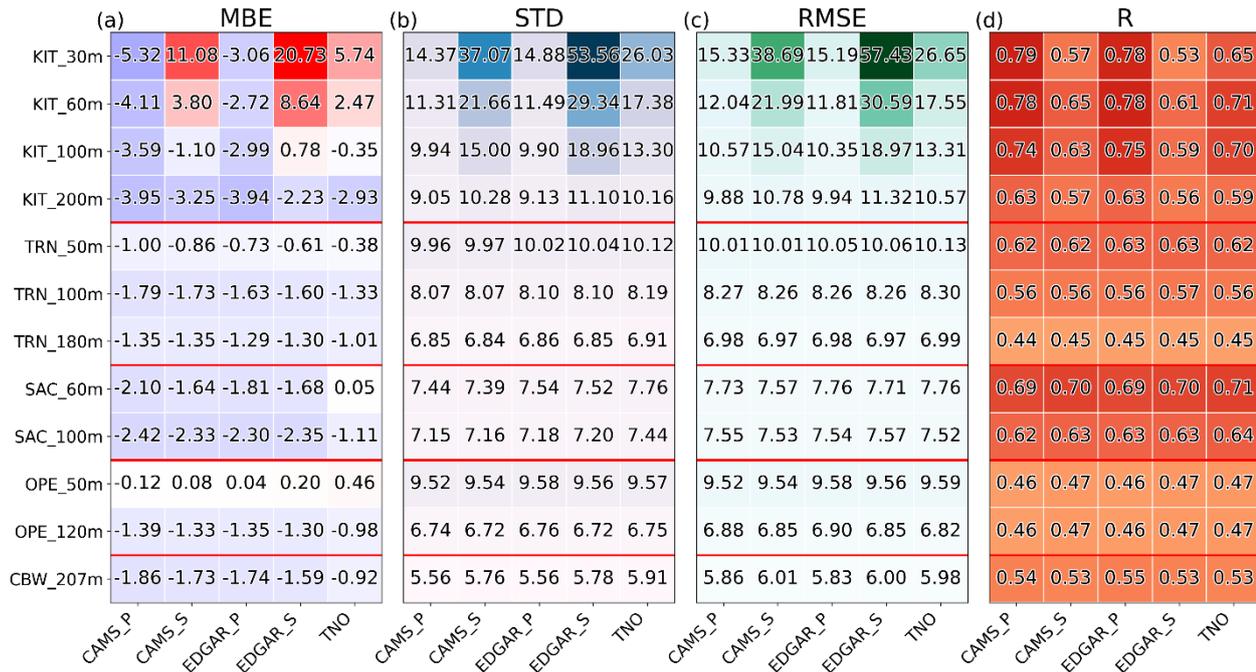

Figure 3. The MBE (a), STD (b), RMSE (c), and R (d) of near surface CO₂ mole fractions between five different simulations and observations at different heights at various ICOS stations. The colors in (a) represent values from negative to positive, with a blue–white–red gradient: negative values in blue, positive values in red, and values near zero in white, whereas in (b–d), more intense colors represent larger values and less intense colors represent smaller values.

At the KIT site, taking into account the vertical distribution of anthropogenic emissions has a significant impact on the simulation results. Simulations using elevated emissions show much better agreement with observations, especially for the lower levels. At the height of 30 m, when using the CAMS-REG-ANT emission inventory and considering elevated emissions, the model-observation bias has a low MBE of -5.32 ppm, a STD of 14.37 ppm, a RMSE of 15.33 ppm, and high correlation R of 0.79. When only surface emissions are considered, MBE, STD, and RMSE increase significantly to 11.08 ppm, 37.07 ppm, and 38.69 ppm, respectively, and R drops to 0.57. The simulations using EDGAR v2024 display similar characteristics, with

12

even larger differences between elevated emissions and surface emissions. As shown in Fig. 4(i-l), compared to simulations accounting for elevated emissions, the simulations that only consider surface emissions tend to overestimate CO_2 mole fractions at 30 m, 60 m and 100 m heights. Their diurnal cycles (Fig. 4(a–h)) indicate that all five simulations are able to capture the diurnal variation of CO_2 and reproduce the lower CO_2 mole fractions well in the afternoon, but the simulation considering only surface emissions significantly overestimates higher CO_2 mole fractions in the morning, leading to large discrepancies with the observations. This overestimation is especially pronounced when using the EDGAR inventory. However, at the other four observation sites (TRN, SAC, OPE, CBW), the differences among the five simulation results are relatively small, and the simulations considering only surface emissions do not show a significant overestimation (see Fig. A2). The discussion in Sect. 5.1 will provide a more detailed analysis of this phenomenon.
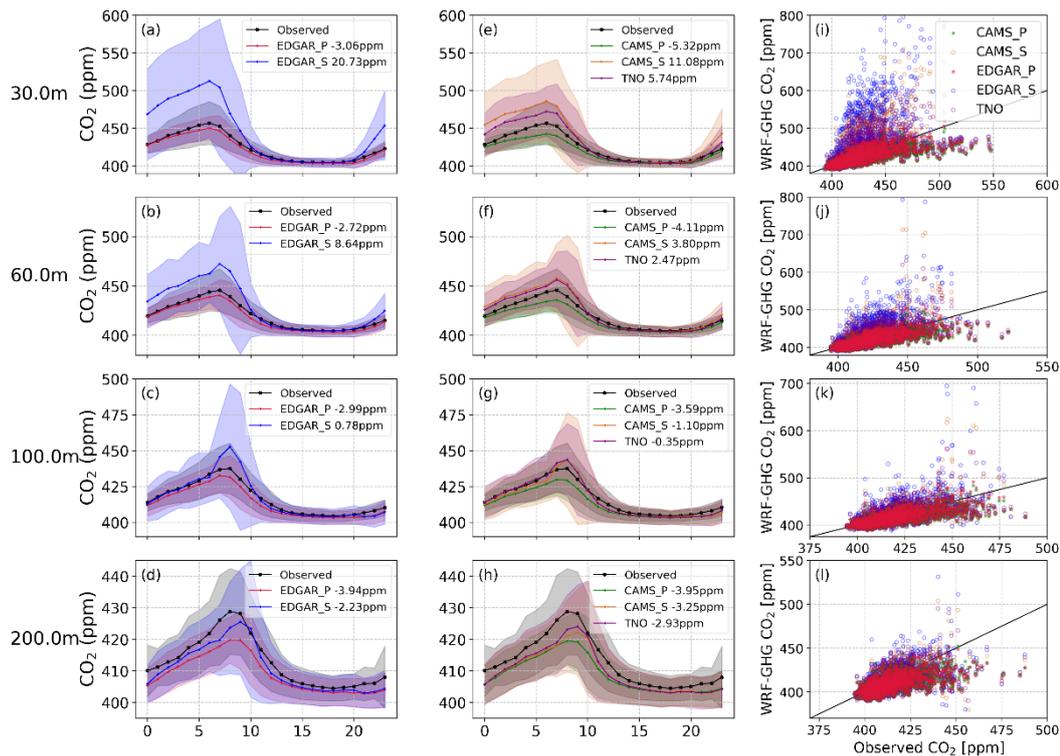
Figure 4. Diurnal cycles (local time) of simulations with different anthropogenic emissions and observations (a-h), where the values represent the MBE between each simulation and observations, along with scatterplots comparing each simulation to the observations (i-l) at different heights at the ICOS KIT site.

As shown in Fig. 5, the contributions from biomass burning and oceanic sources to the diurnal cycles are negligible at these five sites. At the KIT, SAC and CBW sites, the diurnal variability of near-surface CO_2 mole fractions is mainly driven by local anthropogenic emissions and biogenic processes, with the biogenic signal systematically stronger. The diurnal variation of anthropogenic CO_2 is attributed to planetary boundary layer (PBL) dynamics and regional transport. Between 15:00 and 17:00 in the afternoon, the PBL (see Fig. A3) reaches its maximum height, coinciding with the minimum anthropogenic CO_2 mole

13

fractions. After sunset, the PBL gradually decreases and remains shallow from midnight until sunrise, leading to the accumulation of anthropogenic emissions. The mole fractions of CO_2 increase during this period and typically peak between

330   06:00 and 10:00 in the morning. As the PBL rises again after sunrise and turbulent mixing emerges, CO_2 mole fractions begin to decrease, forming a distinct diurnal cycle. The diurnal variation of biogenic processes is driven by vegetation photosynthesis during the day and respiration at night. Biogenic processes are the dominant drivers of the CO_2 mole fractions at the OPE and TRN sites. These results align with Storm et al. (2023), which found that in the summer of 2020, the biogenic flux signals at most ICOS sites were stronger than anthropogenic emissions, and the largest signal is associated with cropland.
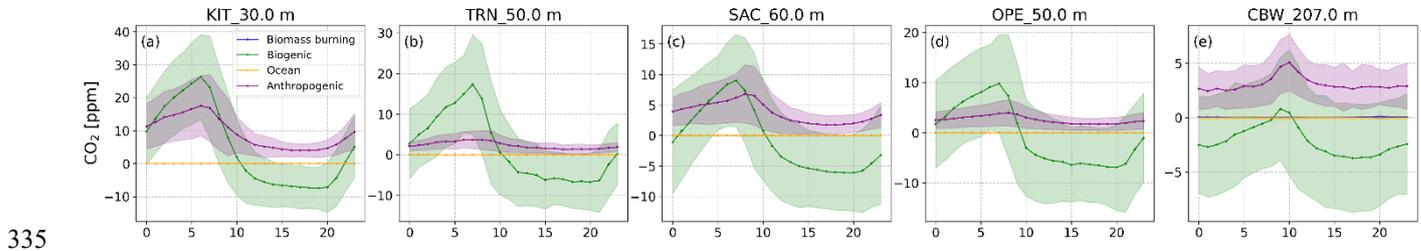

335

Figure 5. Diurnal cycles (local time) of simulated tracer contributions at 30 m at the KIT (a), 50 m at the TRN (b), 60 m at the SAC (c), 50 m at the OPE (d) and 207 m at the CBW (e) sites. Here, the anthropogenic emissions are based on EDGAR v2024, taking into account the vertical emission profiles.

4.2.2 Comparison with TCCON – XCO₂

340   Figure 6b shows the time series of observed and simulated XCO_2 at three TCCON sites, Figure 6c is the corresponding scatterplot, with N representing the number of data pairs, and Figure 6a shows the differences between simulations and observations at each site. Here the simulations are based on the TNO inventory. Due to the lack of observational data at the Paris and Karlsruhe sites in June, the number of valid data pairs for comparison with the simulations is only 123 and 243, respectively. It is obvious that at the Orléans site, the simulated XCO_2 values show a significant underestimation in early June,

345   which will be discussed in detail in the following section.

The statistical metrics between the simulated XCO_2 using five different anthropogenic emission inputs and observed XCO_2 at the three TCCON sites are given in Fig. 7. Among the three sites, the choice of emission inventory has the largest impact on the simulations at the Paris site. At this site, the difference in simulated XCO_2 between using the EDGAR and TNO inventories reaches 0.50 ± 0.34 ppm. Among the five sensitivity tests, all the simulations show an overestimation, with MBEs around 1.2

350   ppm, and up to 1.65 ppm when using TNO. An inspection of the different tracer contributions to XCO_2 (see Fig. 8) indicates that despite uncertainties in the estimation of biogenic carbon fluxes, the overestimation of background XCO_2 from the CAMS and anthropogenic emissions plays a dominant role in causing biases in the simulated XCO_2. During the period from late July to early August, the simulations show an overestimation, consistent with the relatively large contribution from anthropogenic tracers during that period. These results indicate that the uncertainty in anthropogenic emission inventories remains relatively

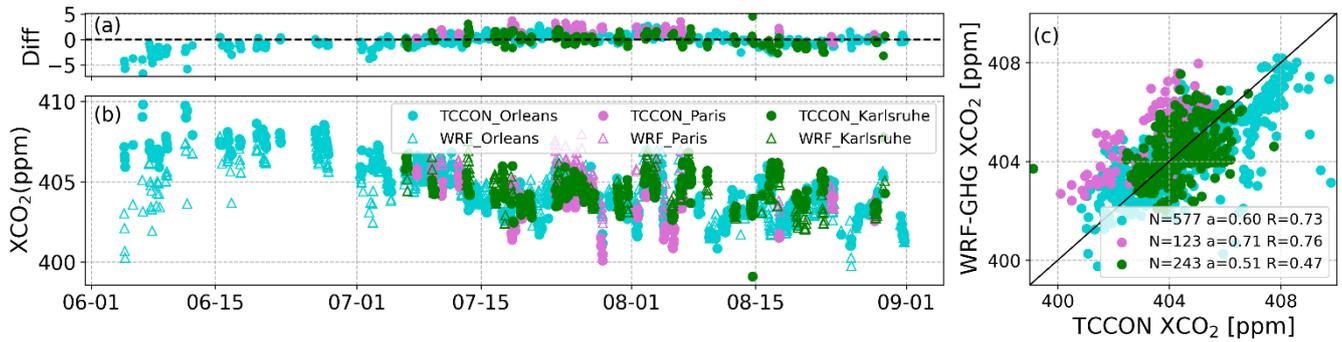355   high in urban areas (Gately and Hutyra, 2017; Super et al., 2020).

Figure 6. Time series (local time) of simulated XCO_2 using TNO inventory and observed XCO_2 at three TCCON sites (b), their absolute differences (WRF-GHG - TCCON) (a), and scatterplots (c). "N" represents the number of data pairs, "a" represents the slope of the linear regression curve and "R" represents the correlation coefficient.

360

Additionally, as XCO_2 is less sensitive to vertical transport processes (Wunch et al., 2011), one expects less impact of considering elevated anthropogenic emissions heights on the simulation results for XCO_2. Indeed, at the Orléans and Paris sites, the impact is negligible for a given emission inventory, while at the Karlsruhe site, we observe a small improvement in the simulation of XCO_2 but not as notable as that observed for near-surface mole fractions. At the Karlsruhe site, when

365 accounting for elevated emission heights in the CAMS-REG-ANT inventory, the STD and RMSE of differences between simulations and observations improves from 1.13 ppm to 1.05 ppm and 1.06 ppm, respectively while R increases from 0.44 to 0.47; for EDGAR, STD and RMSE decrease from 1.16 ppm to 1.03 ppm and 1.04 ppm, respectively, while R increases from 0.43 to 0.48.

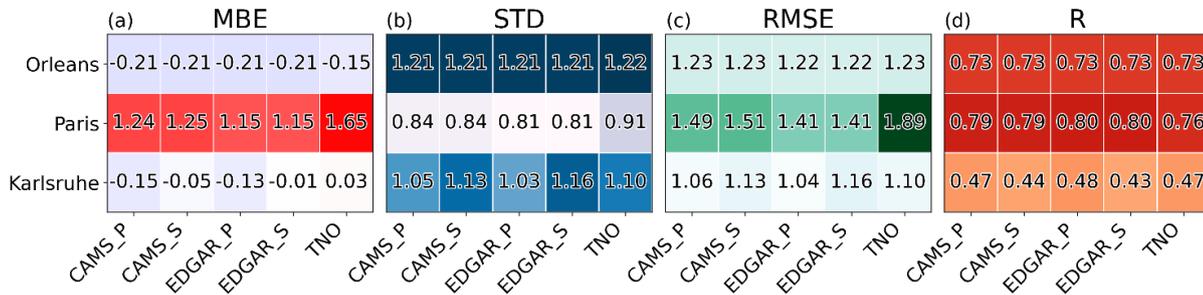370 **Figure 7.** The MBE (a), STD (b), RMSE (c), and R (d) of XCO_2 between five different simulations and observations at three TCCON stations.
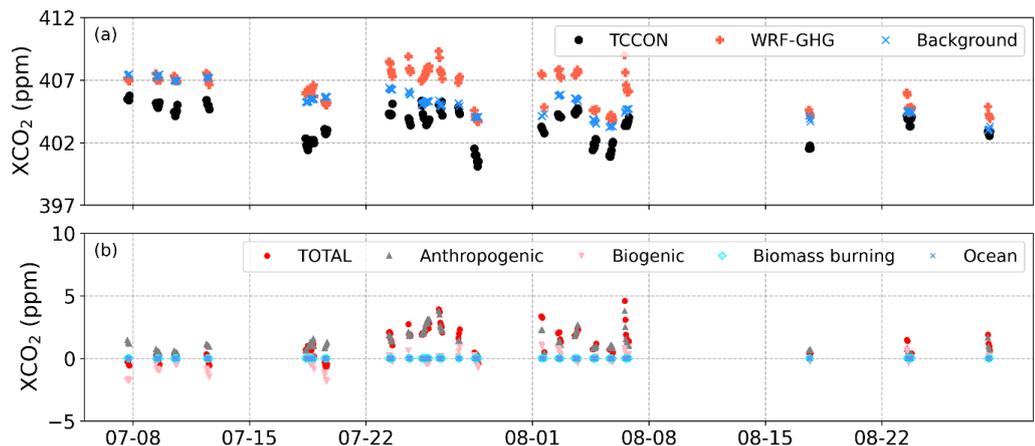
Figure 8. Time series (local time) of (a) observed and simulated total, background, and (b) tracer-specific XCO₂ at Paris site. The simulated values here are all without AVK smoothing.

5 Discussion

We will first discuss the anthropogenic emissions sensitivity tests results and then focus on the biogenic fluxes impacts on model biases reported in June 2018.

### 5.1 Impact of taking into account the height of anthropogenic emissions

As previously noted, at the KIT site, whether anthropogenic emissions are released according to source-specific vertical profiles or only at the surface has a significant impact on the simulation of near-surface CO_2 mole fractions, and also shows a slight influence on XCO_2. Such large impacts are not observed at the other sites.
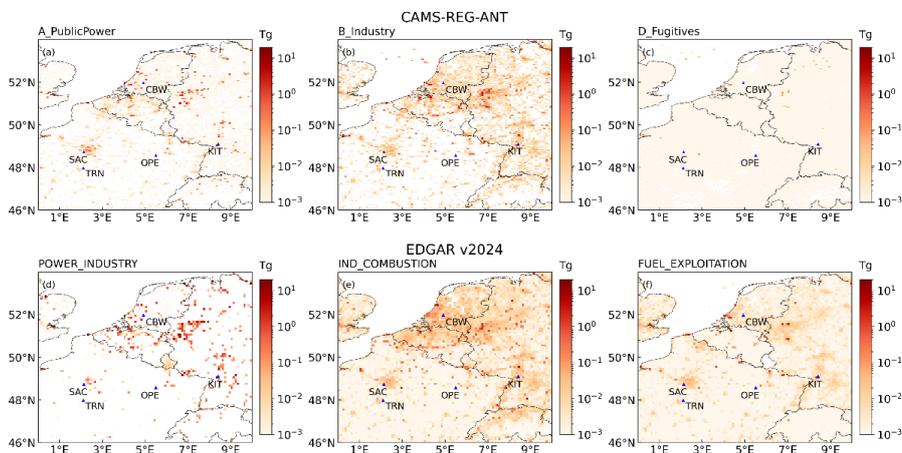
Figure 9. The maps of sector-specific CO2 emissions for 2018 from CAMS-REG-ANT (a) public power, (b) industry and (c) fugitives sectors, and EDGAR v2024 (d) power industry, (e) industrial combustion and (f) fuel exploitation. All values are shown on a logarithmic scale (base 10, unit: Tg).

16

Figure 9 shows the 2018 emission maps of the major contributing sectors from two inventories, including the Public Power (SNAP 1), Industry (SNAP 3) and Fugitives (SNAP 5) sectors from CAMS-REG-ANT, and the Power Industry (SNAP 1), Industrial Combustion (SNAP 3) and Fuel Exploitation (SNAP 5) sectors from EDGAR. Although monthly EDGAR emission data for 2018 were used in the simulations, in these maps the monthly EDGAR inventories were aggregated by summing over all months to produce an annual emission inventory for 2018 for enabling comparison with the CAMS-REG-ANT inventory. It is clearly evident that, except for Industrial Combustion, there are large emission sources near the KIT site, as well as near the CBW and SAC sites, whereas there are almost no emission sources in the vicinity of the TRN and OPE sites. Figure A4 shows the diurnal cycles of the five near-surface CO_2 mole fractions at each ICOS site as simulated by WRF-GHG fractions at the lowest model level (approximately 25 m above ground level). It can be found that at the TRN and OPE sites, the five simulations show nearly identical patterns, consistent with the relatively weak anthropogenic emissions in their surrounding areas. In contrast, at the SAC and CBW sites, whether vertical emissions are taken into account does indeed affect the simulations. However, at the observation heights of these two sites, the impact is small and does not exhibit characteristics similar to those observed at the KIT site. For the SAC site, this may be due to the relatively weaker emission sources nearby, whereas for the CBW site, this may be related to the relatively high observation height used (207 m above ground level), as shown for the KIT site (Fig. 4), the discrepancies between sensitivity tests decrease with increasing observation height.

According to Google Maps, we found that approximately 6.5 km southwest in a straight line from the KIT observation site lies the largest oil refinery of Germany (Junkermann et al., 2011), and about 45 km north of the site there is a gas-fired combined heat and power (CHP) plant located within the Badische Anilinund Sodafabrik (BASF) chemical production facility in Ludwigshafen, Germany. These two are likely the main contributors to the emissions in the inventory near KIT site.

In addition, based on footprint simulations from the regional Stochastic Time-Inverted Lagrangian Transport (STILT) model (Lin et al., 2003), we calculated the aggregated footprints for each afternoon hour (14:00 LT) over the simulation period (not shown here). The results show that, centered on the KIT site, at least 80% of CO_2 enhancements from anthropogenic emissions are covered within a radius of approximately 1.5°. Therefore, we calculated the CO_2 emission fluxes from the sectors corresponding to those in Fig. 9 in 2018, within the area surrounding the KIT site, bounded by 47.6°N to 50.6°N and 6.94°E to 9.94°E (see Fig. 10a). For consistency, the SNAP sector classification is used here. The vertical emission profiles applied for the corresponding sectors are given in Fig. 10b, and the complete vertical profiles for all sectors can be found in Fig. 2a of Brunner et al. (2019). For the EDGAR inventory, emissions from sector SNAP 1 are the dominant source, with the emission flux in 2018 as high as 52.18 Tg, and for the CAMS-REG-ANT inventory, emissions from sectors SNAP 1 and SNAP 3 are the main sources, with fluxes of 24.39 Tg and 32.35 Tg, respectively. According to their respective vertical emission profiles, emissions from SNAP 1 and SNAP 3 are primarily concentrated at higher altitudes. In particular, the emission profile of SNAP 1 begins at approximately 150 meters above ground level, without emissions near the surface. This can explain the finding that in Sect. 4.2.1 at the KIT 30 m height, the difference between tests S and P is larger for EDGAR v2024 than for CAMS-REG-ANT.

17

420 In summary, at KIT, where anthropogenic emissions are significant, SNAP 1 and SNAP 3 are the dominant emissions sectors explaining the improvement of the simulation results by including vertical emissions profiles. Considering anthropogenic vertical profile emissions in the model setup significantly improve the simulations performance, especially in the vicinity of large sources.
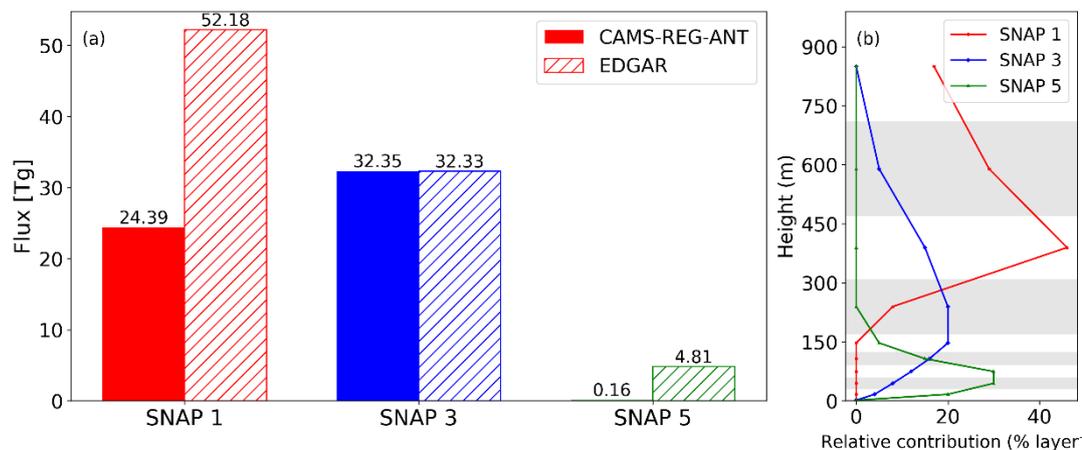
425 **Figure 10. (a) CO_2 emission fluxes from different sectors in 2018 within the area (47.6°N - 50.6°N, 6.94°E - 9.94°E) surrounding the KIT site, and (b) the vertical emission profiles applied for the corresponding sectors, the height refers to the altitude above ground level.**

5.2 Underestimation of model CO_2 simulations in early June

A significant underestimation of the simulated XCO_2 was found at the Orléans site in early June. According to the contributions

430 of each tracer to the total simulated XCO_2 (see Fig. 11), a similar pattern is found in the biogenic component. Additionally, a comparison between simulated and observed near-surface CO_2 mole fractions at various heights from the co-located ICOS TRN site also reveals a clear underestimation in early June (Fig. A5). This site pair is hereafter referred to as Orléans/TRN. Figure 11c shows the vertical distribution of the biogenic CO_2 tracer at Orléans/TRN over time, revealing a sink spanning a large vertical extent in early June. At the other two TCCON sites (Paris and Karlsruhe), due to the lack of observational data

435 in June, it is difficult to determine whether a similar feature exists. However, the underestimation of CO_2 mole fractions in early June is not confined to the Orléans/TRN site. A consistent underestimation during this period is also observed at the other ICOS sites (OPE, SAC, CBW, see Fig. A5), except for the KIT site which includes significant anthropogenic emissions, indicating that this is likely a regional feature rather than a localized effect at a single site. In addition, the STILT simulation results published on the ICOS Carbon Portal also exhibit an underestimation at these ICOS sites (except for the KIT site) in

440 early June. The biospheric fluxes are from the VPRM model (Gerbig and Koch, 2023), with VPRM parameters optimized for the year 2007 using 46 sites across Europe, and the land cover classification is based on SYNMAP.
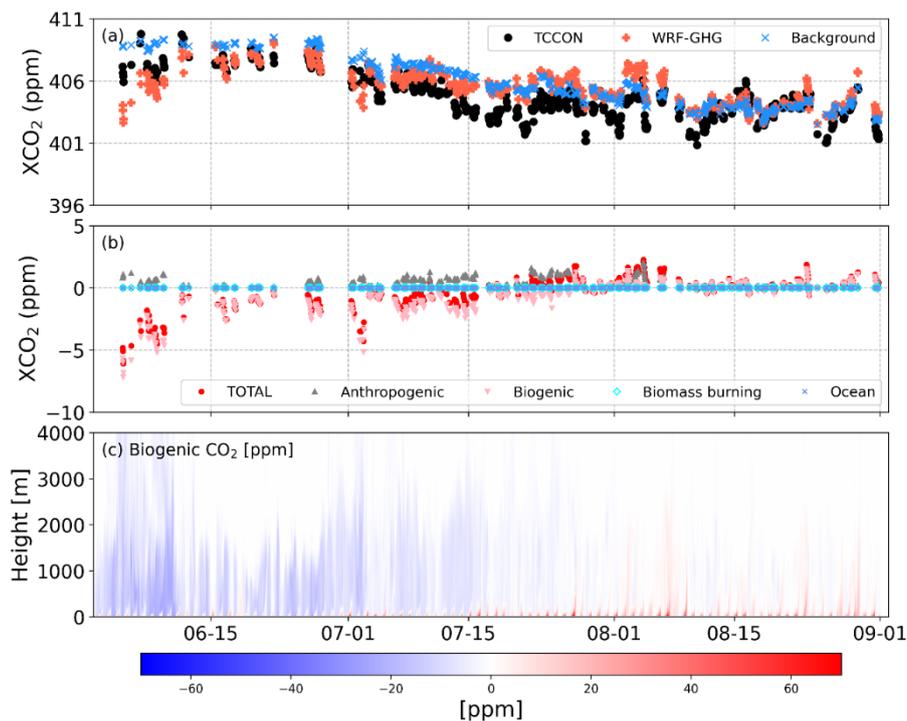
Figure 11. Time series (local time) of (a) observed and simulated total, background, (b) tracer-specific XCO₂, and (c) variation of simulated biogenic CO₂ mole fractions over time (local time) and height above ground at Orléans/TRN site. The simulated values here are all without AVK smoothing.

At most ICOS and TCCON sites included in this study, GPP and daytime NEE in June exhibit a stronger carbon sink compared to July and August. Starting from July, LSWI and EVI values, which are used as input to VPRM, across all vegetation types declined significantly, reflecting an overall decrease in vegetation activity and greenness. This trend was observed at the Orléans/TRN site (see Fig. A6), and similar patterns were found at other sites. This could be attributed to a prolonged and intense drought that occurred in Europe during the summer of 2018. This event directly affected temperature, soil moisture, precipitation, and ecosystem functioning (Buras et al., 2020). Simulations by WRF-GHG and VPRM, driven by meteorological fields and vegetation indices, both responded to this drought event.

Regarding the mismatch between the model and observations in early June, the simulated NEE shows a pronounced carbon sink at most sites. Unfortunately, the lack of co-located flux measurements at these atmospheric observation sites limits the direct evaluation of flux accuracy. Alternatively, we evaluated the four ICOS flux stations within the model's inner domain: two sites in Germany, DE_RuR (50.621914°N, 6.304126°E; grasslands) and DE_RuW (50.50493°N, 6.330963°E; forest), and two in France, FR_EM2 (49.87211°N, 3.02065°E; crops) and FR_LGt (47.322918°N, 2.284102°E; acid fen) (not shown here). The simulated RES shows a significant underestimation at all sites, except at FR_LGt site, which is consistent with Hu et al. (2021), who pointed out that the VPRM model tends to underestimate ecosystem respiration during the growing season, which

19

460 could introduce biases in the simulation of NEE. At the two French sites, the simulated GPP exhibits more gross uptake significantly.

Additionally, we tested four different sets of VPRM parameter settings (not show here), all of which resulted in a similar underestimation in early June, preliminarily ruling out parameter settings as the primary source of the bias. It could rather be the consequences of the limitations either of the model itself.

465 In summary, the underestimation of simulated CO_2 mole fractions observed at multiple ICOS and TCCON sites in early June might be attributed to an underestimation of ecosystem respiration fluxes or an overestimation of GPP. However, owing to the lack of co-located flux measurements, the exact source of this bias remains unclear and requires further investigation.

6 Conclusion

In this study, we performed the first high-resolution simulation of the spatiotemporal distribution of CO_2 mole fractions over
470 Western Europe during the summer (June to August) of 2018 using WRF-GHG. Given the significance of anthropogenic emissions and the diversity of emission inventories, we conducted several sensitivity tests and evaluated the model performance from both meteorological and chemical field perspectives by comparing with ground-based observations at multiple synoptic, ICOS and TCCON stations, on the purpose of optimizing the modelling set-up and - at a later stage - analyzing the CO_2 concentration variations over Belgium and surrounding countries systematically, ultimately offering a solid
475 basis for related modelling and applied studies.

Overall, the WRF-GHG model reproduces the meteorological fields well, especially temperature, with high Pearson correlation coefficients ranging from 0.92 to 0.96 against observations from various synoptic sites. The model can capture the variations of wind speed at different heights, on both daily and monthly timescales. At inland stations, the model tends to overestimate wind speeds at most sites with dense vegetation cover, while it generally underestimates near airports or in areas dominated
480 by cropland. These discrepancies highlight the importance of accurate and high-spatial-resolution land-cover maps for the reproduction of transport processes. Moreover, the diurnal variation of near-surface CO_2 mole fractions at different heights across the five ICOS observation sites was well captured by the model. During the summer 2018, variations in CO_2 mole fractions over Belgium and surrounding countries were mainly influenced by anthropogenic emissions and biogenic fluxes.

Sensitivity tests indicate that near large anthropogenic emission sources, the simulated near-surface CO_2 mole fractions are
485 highly sensitive to the choice of anthropogenic emission inventory and the adoption of vertical emission profiles. At the KIT site in Germany, which is located near a very large oil refinery and power plant, differences between emission inventories can lead to discrepancies of up to 14.99 ± 31.98 ppm in simulated near surface CO_2 mole fractions. In addition, releasing anthropogenic emissions based on source-specific vertical profiles can significantly improve the accuracy of simulations, which is likely due to a more realistic representation of the real emissions. In contrast, at other observation sites where
490 surrounding anthropogenic emissions are relatively low, the impact of vertical emission profiles on simulation results is much smaller.

Regarding XCO_2, the model seems to be less sensitive to the choice of emission inventories and anthropogenic emission heights, but certain effects are still evident. At the Paris urban site, all simulations overestimate XCO_2 by approximately 1.2-1.6 ppm. This bias is primarily attributed to the uncertainties introduced by anthropogenic emissions and using CAMS data as initial and boundary conditions. In addition, the differences caused by different anthropogenic emission inventories can reach up to 0.50 ± 0.34 ppm. Although it is less pronounced than for the near-surface mole fractions at the ICOS site, the simulation results confirm that considering vertical emission profiles leads to a modest improvement in model simulations at the Karlsruhe site.

Additionally, biogenic fluxes contribute significantly to CO_2 mole fractions during the growing season. The large negative bias observed in WRF-GHG simulations of CO_2 mole fractions in early June at most ICOS and TCCON sites may be attributed to the underestimation of RES or the overestimation of GPP by the VPRM model. However, due to the lack of flux observations, the exact cause remains uncertain.

This study systematically characterizes and evaluates the distribution of CO_2 concentrations across multiple observational sites, with a particular focus on regions surrounding Belgium, demonstrates the feasibility of using the WRF-GHG model to simulate CO_2 concentration variations in the core region of Western Europe, and provides a basis for applying this model to the study of other long-lived greenhouse gases like CH_4 and N_2O in this region demonstrates the feasibility of using the WRF-GHG model to simulate CO_2 concentration variations in the core region of Western Europe, and provides a basis for applying this model to the study of other long-lived greenhouse gases like CH_4 and N_2O in Western Europe. It further emphasizes the importance of optimizing initial and boundary conditions and refining the construction of source-specific vertical emission profiles to enhance simulation accuracy. However, to further improve simulation accuracy, future efforts should focus on optimizing initial and boundary conditions and refining the construction of source-specific vertical emission profiles. Additionally, due to the relatively simplified e parameterization of the current VPRM, its applicability across different climatic conditions remains limited it may not perform well under all conditions, whether under normal climate or extreme stress. Nonlinear ecosystem responses under extreme temperature and moisture conditions may lead to biases in simulated respiration fluxes For example, biases in respiration fluxes may arise from nonlinear ecosystem responses to extreme temperature and moisture conditions, which indirectly reflect the complexity of the biosphere-atmosphere system under extreme environmental stress and indicate that which are not accounted for in the model. Therefore, a modified VPRM model is necessary (Gourdji et al., 2022). At the same time, this study highlights the critical role of observations in evaluating regional simulations and supporting the understanding of carbon emissions and the distribution of CO_2 concentrations in the atmosphere observational data play a critical role in model evaluation, as the availability of time-synchronized ground-based observations of CO_2 fluxes and concentrations can help assess the performance of the model, thereby enhancing the credibility and scientific interpretation of the simulation results. Overall, this work not only advances the understanding of the spatiotemporal variations of CO_2 in the core region of Western Europe, but also provides an important reference for developing more reliable regional-scale carbon-climate feedback modelling tools, thereby contributing to a deeper understanding of the interactions between extreme climate and the carbon cycle.

Appendix

Table A1. Overview of the VPRM parameters. The temperature parameters are all in degrees Celsius. The abbreviations are as follows: EF - evergreen forest, DF - deciduous forest, MF - mixed forest, SHR - shrubland, WET - wetland, CRO - cropland, GRA - grassland.

		Tmin	Topt	Tmax	Tlow	λ	Par0	α	β
1	EF	-4	15	38	-3	-0.26	263.60	0.21	1.15
2	DF	1	21	37	0	-0.26	252.90	0.23	1.26
3	MF	-1	18	38	0	-0.28	227.81	0.19	0.93
4	SHR	-1	19	44	2	-0.20	224.27	0.08	0.56
5	WET	-2	26	40	0	-0.24	201.85	0.3	-0.39
6	CRO	-3	16	50	-3	-0.18	485.20	0.17	1.14
7	GRA	-2	17	36	-2	-0.44	223.92	0.27	1.63
8	OTHER	0	0	0	0	0	0	0	0

530

Table A2. Sector mapping between different emission inventories (Granier et al., 2019)

| SNAP	CAMS-REG-ANT (GNFR)	EDGAR v2024
1 Energy industry	A Public Power	Power Industry
2 Non-industrial combustion	C Other Stationary Comb	Buildings
3 Combustion in manufacturing industry	B Industry	Industrial combustion
4 Production processes		Processes
5 Extraction of fossil fuels	D Fugitive	Fuel exploitation
6 Product use	E Solvents	
7 Road transport	F Road Transport	
8 Non-road transport	G Shipping H Aviation I Offroad	Transport
9 Waste treatment	J Waste	Waste
10 Agriculture	K Agrilivestock L AgriOther	Agriculture

Table A3. Evaluation metrics for temperature, wind speed, and wind direction between simulations and observations at the 21 synoptic stations. The eight stations marked with * are operated by Skeyes and Meteo Wing, where wind speed and wind direction observations are recorded only as integer values. The four stations marked with ^c represent coastal sites.

535

Site	Location	Temperature					Wind Speed					Wind Direction				
		N	MBE	STD	RMSE	R	N	MBE	STD	RMSE	R	N	MBE	STD	RMSE	R

6400*c	51.088 ° N 2.652°E	2200	-0.24	1.27	1.29	0.95	2201	-0.32	1.36	1.40	0.75	2201	-1.14	51.56	51.57	0.61
6407*c	51.200°N 2.887°E	2202	-0.11	1.84	1.84	0.92	2202	-1.19	1.65	2.04	0.67	2202	3.40	37.29	37.45	0.67
6414	50.904°N 3.122°E	2180	-0.63	1.56	1.68	0.95	2180	0.21	1.13	1.15	0.75	2149	5.38	36.05	36.46	0.58
6418c	51.347°N 3.202°E	2135	-0.38	1.31	1.36	0.93	2134	-2.42	1.55	2.88	0.74	2134	4.99	32.29	32.68	0.68
6434	50.980°N 3.816°E	2202	-0.50	1.63	1.71	0.95	2202	0.40	1.16	1.22	0.72	2123	0.47	41.14	41.15	0.58
6438c	51.325°N 4.364°E	2189	-0.14	1.47	1.48	0.95	2189	-0.56	1.27	1.39	0.70	2100	7.38	39.57	40.25	0.61
6439	51.075°N 4.525°E	1624	0.19	1.40	1.41	0.96	1621	-0.20	0.91	0.93	0.77	1523	4.19	41.10	41.32	0.50
6447	50.797°N 4.358°E	2202	0.06	1.42	1.42	0.95	2202	-0.37	0.96	1.03	0.69	2193	4.90	40.50	40.81	0.62
6449*	50.454°N 4.442°E	2202	0.30	1.53	1.56	0.95	2202	-0.98	1.14	1.50	0.69	2096	4.00	37.09	37.31	0.56
6450*	51.191°N 4.452°E	2202	0.01	1.41	1.41	0.95	2202	-1.07	1.20	1.61	0.69	2072	-5.15	38.94	39.29	0.62
6451*	50.896°N 4.527°E	2202	0.99	1.46	1.76	0.95	2202	-0.82	1.21	1.46	0.68	2064	-4.61	38.67	38.94	0.60
6455	50.095°N 4.595°E	2202	-0.29	1.86	1.89	0.94	2202	0.72	1.08	1.30	0.61	1984	10.96	53.46	54.52	0.48
6459	50.582°N 4.689°E	2202	-0.06	1.48	1.49	0.96	2202	0.15	1.17	1.18	0.71	2183	15.95	40.30	43.34	0.49
6464	51.221°N 5.027°E	2202	-0.45	1.58	1.65	0.96	2202	0.98	1.12	1.49	0.59	1918	8.15	41.60	42.40	0.50
6472	50.194°N 5.255°E	2202	0.23	1.72	1.73	0.94	2202	0.23	1.10	1.12	0.74	2149	9.15	49.61	50.46	0.50
6476*	50.039°N 5.404°E	2202	-0.19	1.49	1.50	0.95	1627	0.09	1.15	1.16	0.71	1497	-1.32	40.81	40.84	0.65
6477	50.915°N 5.450°E	2202	-0.38	1.89	1.93	0.94	2202	0.43	1.18	1.26	0.69	2029	0.86	47.55	47.55	0.54
6478*	50.645°N 5.459°E	2202	0.43	1.46	1.52	0.95	2200	-0.72	1.18	1.38	0.71	2084	4.98	43.18	43.48	0.58
6484	49.620°N	1147	0.42	1.98	2.02	0.94	1147	0.44	1.26	1.34	0.47	1137	-19.34	56.21	59.47	0.48

	5.587°E															
6490*	50.479°N 5.910°E	2183	-0.15	1.54	1.55	0.95	2174	0.35	1.24	1.29	0.65	2019	-4.65	46.05	46.29	0.47
6494	50.511°N 6.073°E	2121	-0.19	1.49	1.51	0.95	2126	0.78	1.03	1.30	0.71	2105	9.10	41.32	42.32	0.55
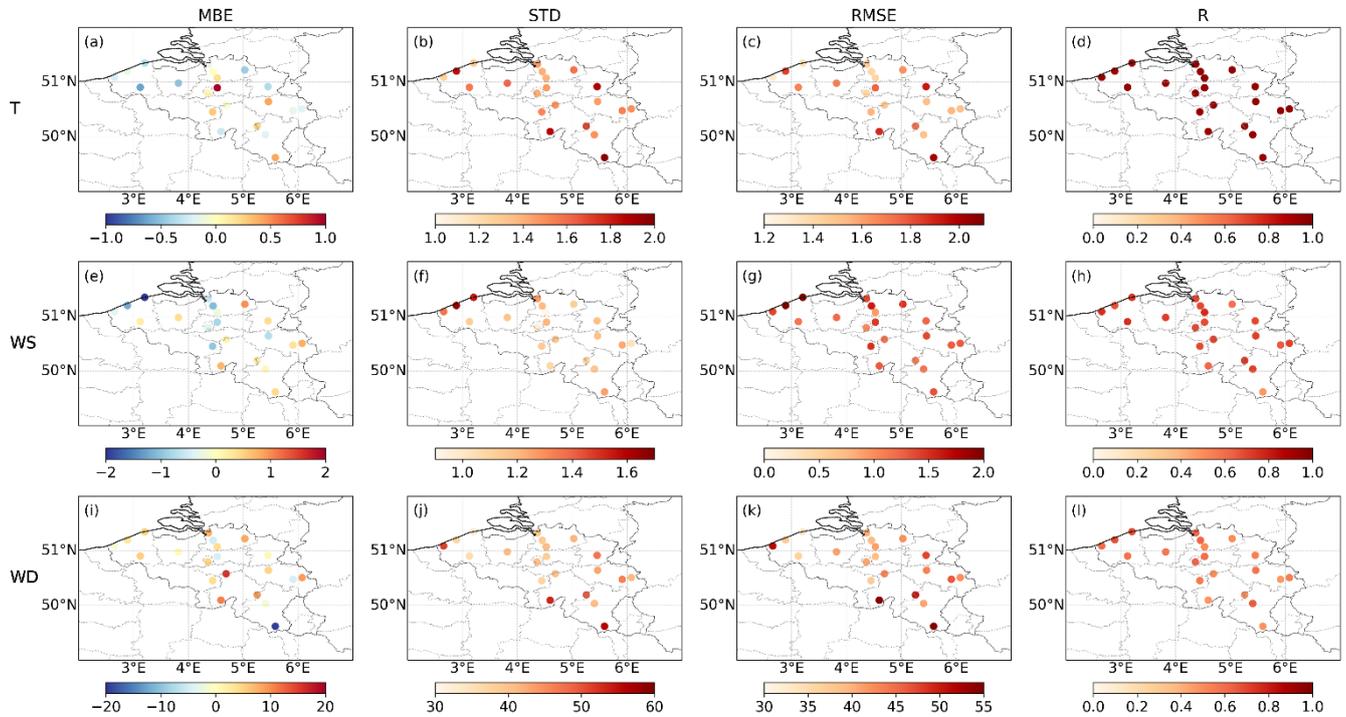
Figure A1. Map of evaluation metrics for temperature (a-d), wind speed (e-h), and wind direction (i-l) between simulated and observed values at 21 synoptic stations.
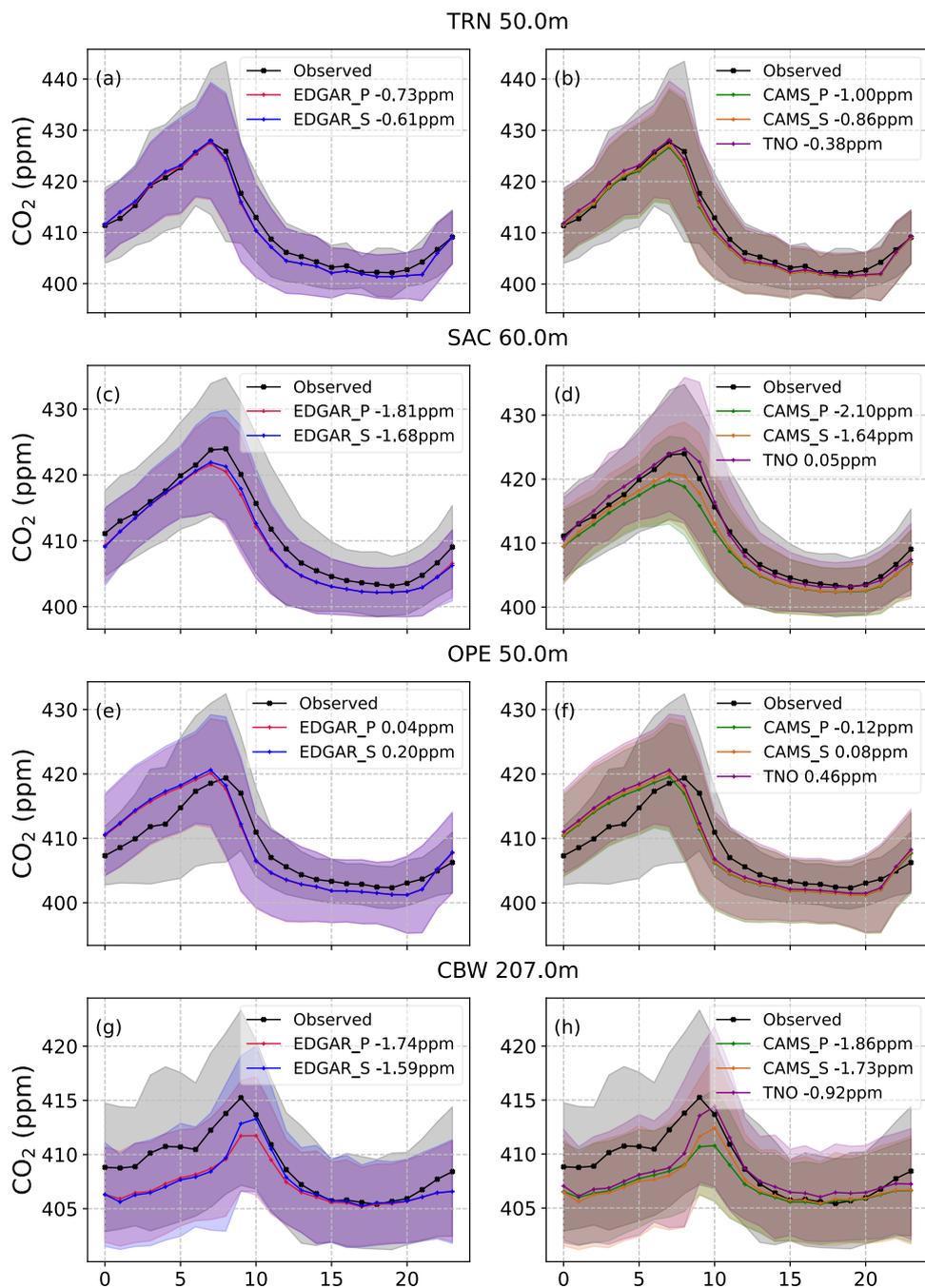
Figure A2. Diurnal cycles (local time) of simulations with different anthropogenic emissions and observations at 50 m at the TRN (a, b), 60 m at the SAC (c, d), 50 m at the OPE (e, f) and 207 m at the CBW (g, h) sites, where the values represent the MBE between each simulation and observations .
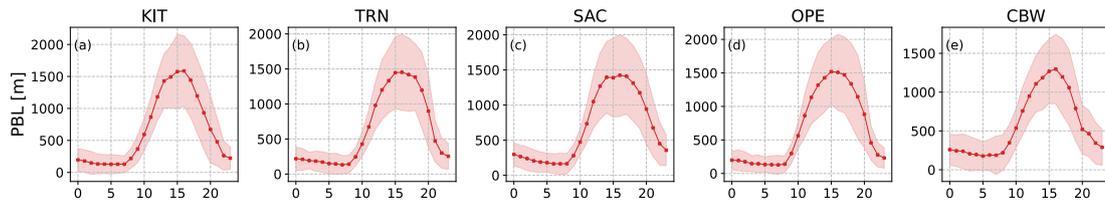
Figure A3. The diurnal cycles (local time) of planetary boundary layer height simulated by WRF-GHG at the KIT (a), the TRN (b), the SAC (c), the OPE (d) and the CBW (e) sites.
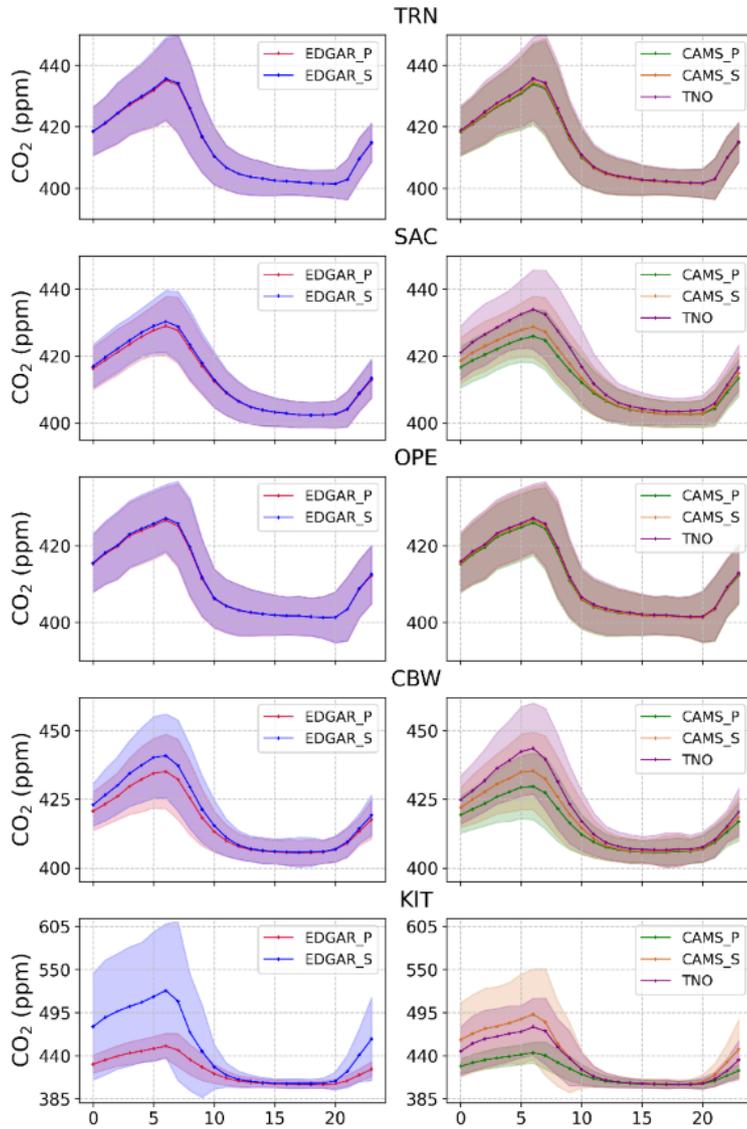
Figure A4. Diurnal cycles (local time) of simulations with different anthropogenic emissions at five ICOS sites at the model lowest layer (approximately 25 m above the ground).
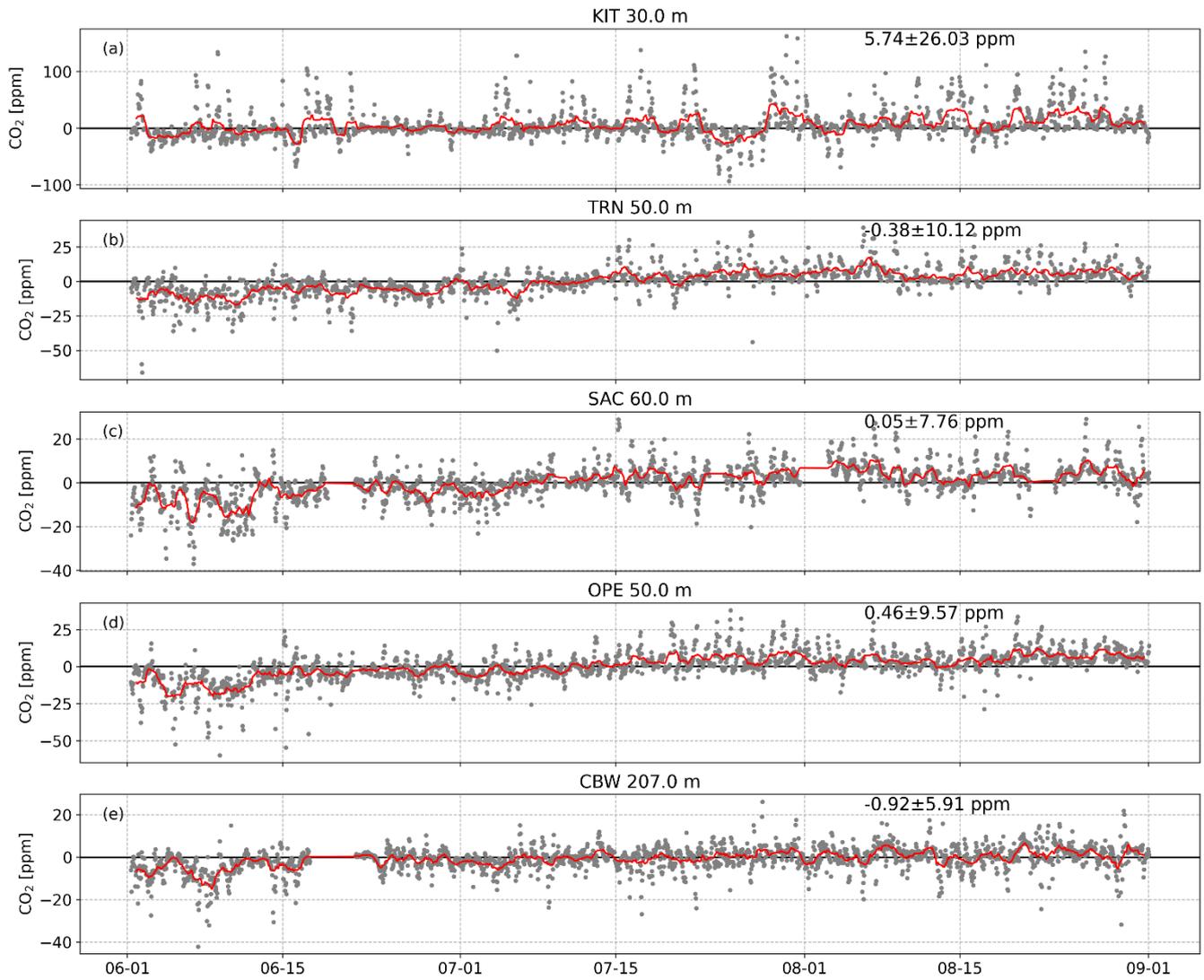
Figure A5. Time series of the between the simulated near surface CO₂ mole fractions using TNO inventory and observed results at 30 m at the KIT (a), 50 m at the TRN (b), 60 m at the SAC (c), 50 m at the OPE (d) and 207 m at the CBW (e) sites, where the values represent the MBE ± STD between the simulations and observations. The red curve represents the 24-hour moving average.
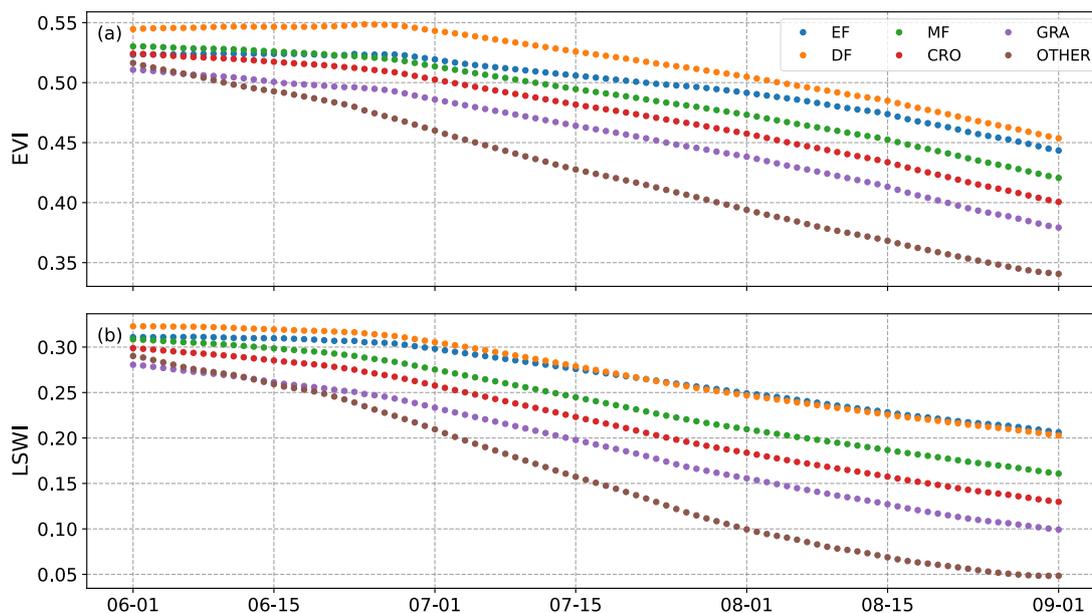
Figure A6. Time series of EVI (a) and LSWI (b) for different vegetation types from MODIS at Orléans/TRN site. According to the land cover data provided by Copernicus, there are no Shrubland (SHR) and Wetlands (WET) vegetation types near Orléans/TRN. Therefore, their corresponding EVI and LSWI values are 0 and are not shown here.

560   **Code and data availability.** The WRF-Chem model code is distributed by NCAR (https://doi.org/10.5065/D6MK6B4K, NCAR, 2020). The model data used to support the results described in this paper are available at https://doi.org/10.18758/7msm8ztv. The synoptic data were downloaded from https://opendata.meteo.be/download, hosted by Royal Meteorological Institute (RMI). ICOS observations are available at https://meta.icos-cp.eu/collections/LKDae89cNpTOKSt1TnK_dRIw (ICOS RI et al., 2023). The TCCON data are available through the

565   TCCON wiki at https://tccondata.org/. The ERA5 dataset is freely accessible after registration from the Copernicus Climate Data Store at https://cds.climate.copernicus.eu/datasets (Hersbach et al., 2020). CAMS global reanalyses, provided by the Copernicus Atmosphere Monitoring Service, were taken from https://ads.atmosphere.copernicus.eu/cdsapp#!/dataset/cams-global-reanalysis-eac4?tab=form (Inness et al., 2019). The CAMS-REG-ANT v8.0 emissions (Kuenen et al., 2022) and temporal profiles CAMS-REG-TEMPO v3.1 (Guevara et al., 2021) are archived and distributed through the Emissions of

570   atmospheric Compounds and Compilation of Ancillary Data (ECCAD) platform. EDGAR emission inventory datasets are available at https://edgar.jrc.ec.europa.eu/dataset_ghg2024 (Crippa et al ., 2024). TNO_GHGco_v4.1 emission inventory was kindly provided by Ingrid Super.

References

Aylas, Y.G.R., De Souza Campos Correa, W., Santiago, A.M., Reis Junior, N.C., Albuquerque, T.T.A., Santos, J.M., Moreira, D.M.: Influence of land use on the performance of the WRF model in a humid tropical climate, Theor. Appl. Climatol., 141, 201–214, https://doi.org/10.1007/s00704-020-03187-3, 2020.

Bastos, A., Ciais, P., Friedlingstein, P., Sitch, S., Pongratz, J., Fan, L., Wigneron, J. P., Weber, U., Reichstein, M., Fu, Z., Anthoni, P., Arneth, A., Haverd, V., Jain, A. K., Joetzjer, E., Knauer, J., Lienert, S., Loughran, T., McGuire, P. C., Tian, H., Viovy, N., and Zaehle, S.: Direct and seasonal legacy effects of the 2018 heat wave and drought on European ecosystem productivity, Sci. Adv., 6, eaba2724, https://doi,org/10.1126/sciadv.aba2724, 2020.

Beck, V., Koch, T., Kretschmer, R., Ahmadov, R., Gerbig, C., Marshall, J., Pillai, D., and Heimann, M.: The WRF Greenhouse Gas Model (WRF-GHG), Technical Report No. 25, techreport 25, Max Planck Institute for Biogeochemistry, https://www.bgc-jena.mpg.de/bgc-systems/uploads/Wrf-ghg/Technical%20Reports%202011%20Beck.pdf (last access: 25 August 2025), 2011.

Bertrand, C., Gonzalez Sotelino, L., and Journée, M.: Quality control of 10-min air temperature data at RMI, Adv. Sci. Res., 10, 1–5, https://doi.org/10.5194/asr-10-1-2013, 2013.

Brunner, D., Kuhlmann, G., Marshall, J., Clément, V., Fuhrer, O., Broquet, G., Löscher, A., and Meijer, Y.: Accounting for the vertical distribution of emissions in atmospheric CO_2 simulations, Atmos. Chem. Phys., 19, 4541–4559, https://doi.org/10.5194/acp-19-4541-2019, 2019.

Buchhorn, M., Smets, B., Bertels, L., De Roo, B., Lesiv, M., Tsendbazar, N., Li, L., and Tarko, A.: Copernicus Global Land Service: Land Cover 100m: Version 3 Globe 2015-2019: Product User Manual, Zenodo, https://doi.org/10.5281/zenodo.3938963, 2020.

Buras, A., Rammig, A., and Zang, C. S.: Quantifying impacts of the 2018 drought on European ecosystems in comparison to 2003, Biogeosciences, 17, 1655–1672, https://doi.org/10.5194/bg-17-1655-2020, 2020.

Callewaert, S., Brioude, J., Langerock, B., Duflot, V., Fonteyn, D., Müller, J.-F., Metzger, J.-M., Hermans, C., Kumps, N., Ramonet, M., Lopez, M., Mahieu, E., and De Mazière, M.: Analysis of CO_2, CH_4, and CO surface and column concentrations observed at Réunion Island by assessing WRF-Chem simulations, Atmos. Chem. Phys., 22, 7763–7792, https://doi.org/10.5194/acp-22-7763-2022, 2022.

Callewaert, S., Zhou, M., Langerock, B., Wang, P., Wang, T., Mahieu, E., and De Mazière, M.: A WRF-Chem study on the variability of CO_2, CH_4 and CO concentrations at Xianghe, China supported by ground-based observations and TROPOMI, EGUsphere [preprint], https://doi.org/10.5194/egusphere-2023-2103, 2023.

Che, G., Zhou, D., Wang, R., Zhou, L., Zhang, H., and Yu, S.: Wind energy assessment in forested regions based on the combination of WRF and LSTM-attention models, Sustainability 16, 898. https://doi.org/10.3390/su16020898, 2024.

Connor, B., Bösch, H., McDuffie, J., Taylor, T., Fu, D., Frankenberg, C., O'Dell, C., Payne, V. H., Gunson, M., Pollock, R., Hobbs, J., Oyafuso, F., and Jiang, Y.: Quantification of uncertainties in OCO-2 measurements of XCO_2: simulations and linear error analysis, Atmos. Meas. Tech., 9, 5227–5238, https://doi.org/10.5194/amt-9-5227-2016, 2016.

Crippa, M., Guizzardi, D., Pagani, F., Banja, M., Muntean, M., Schaaf, E., Monforti-Ferrario, F., Becker, W., Köykkä, J., Grassi, G., Rossi, S., Brandao De Melo, J., Jacome Felix Oom, D., Branco, A., San-Miguel, J., Manca, G., Pisoni, E., Vignati, E., Pekar, F.: EDGAR 2024 Greenhouse Gas Emissions. European Commission, Joint Research Centre (JRC) [Dataset] PID: http://data.europa.eu/89h/88c4dde4-05e0-40cd-a5b9-19d536f1791a, 2024.

Dayal, K. K., Cater, J. E., Kingan, M. J., Bellon, G. D., and Sharma, R. N.: Evaluation of the WRF model for simulating surface winds and the diurnal cycle of wind speed for the small island state of Fiji, J. Phys.: Conf. Ser., 1618, 062025. https://doi.org/ 10.1088/1742-6596/1618/6/062025, 2020.

Della-Marta, P. M., Haylock, M. R., Luterbacher, J. and Wanner, H.: Doubled length of western European summer heat waves since 1880, J. Geophys. Res. 112, D15103, https://doi.org/10.1029/2007JD008510, 2007.

Díaz Isaac, L. I., Lauvaux, T., Davis, K. J., Miles, N. L., Richardson, S. J., Jacobson, A. R., and Andrews, A. E.: Model-data comparison of MCI field campaign atmospheric CO_2 mole fractions, J. Geophys. Res.-Atmos., 119, 10536–10551, https://doi.org/10.1002/2014JD021593, 2014.

Duan, H., Li, Y., Zhang, T., Pu, Z., Zhao, C., and Liu, Y.: Evaluation of the Forecast Accuracy of Near-Surface Temperature and Wind in Northwest China Based on the WRF Model, J. Meteorol. Res 32, 469-490, https://doi.org/10.1007/s13351-018-7115-9, 2018.

Feng, S., Lauvaux, T., Newman, S., Rao, P., Ahmadov, R., Deng, A., Díaz-Isaac, L. I., Duren, R. M., Fischer, M. L., Gerbig, C., Gurney, K. R., Huang, J., Jeong, S., Li, Z., Miller, C. E., O'Keeffe, D., Patarasuk, R., Sander, S. P., Song, Y., Wong, K. W., and Yung, Y. L.: Los Angeles megacity: a high-resolution land atmosphere modelling system for urban CO_2 emissions, Atmos. Chem. Phys., 16, 9019–9045, https://doi.org/10.5194/acp16-9019-2016, 2016.

Gao, B.-C.: NDWI - A Normalized Difference Water Index for Remote Sensing of Vegetation Liquid Water from Space, Remote Sens. Environ., 58, 257–266, 1996.

Gately, C. K. and Hutyra, L. R.: Large Uncertainties in Urban-Scale Carbon Emissions, J. Geophys. Res.-Atmos., 122, 11242–11260, https://doi.org/10.1002/2017jd027359, 2017.

Gerbig, C. and Koch, F.-T.: Biosphere-atmosphere exchange fluxes for CO_2 from the Vegetation Photosynthesis and Respiration Model VPRM for 2006-2022, https://doi.org/10.1016/j.rse.2006.01.020, 2023.

Glauch, T., Marshall, J., Gerbig, C., Botía, S., Gałkowski, M., Vardag, S. N., and Butz, A.: *pyVPRM*: a next-generation vegetation photosynthesis and respiration model for the post-MODIS era, Geosci. Model Dev., 18, 4713–4742, https://doi.org/10.5194/gmd-18-4713-2025, 2025.

Gourdji, S., Karion, A., Lopez-Coto, I., Ghosh, S., Mueller, K. L., Zhou, Y., Williams, C. A., Baker, I. T., Haynes, K., and Whetstone, J.: A modified Vegetation Photosynthesis and Respiration Model (VPRM) for the eastern USA and Canada, evaluated with comparison to atmospheric observations and other biospheric models, J. Geophys. Res.-Biogeo., 127, e2021JG006290, https://doi.org/10.1029/2021JG006290, 2022.

Granier, C., Darras, S., Denier van der Gon, H., Doubalova, J., Elguindi, N., Galle, B., Gauss, M., Guevara, M., Jalkanen, J.-P., Kuenen, J., Liousse, C., Quack, B., Simpson, D., and Sindelarova, K.: The Copernicus Atmosphere Monitoring Service Global and Regional Emissions (April 2019 Version), https://atmosphere.copernicus.eu/sites/default/files/2019-06/cams_emissions_general_document_apr2019_v7.pdf (last access: 6 May 2025), 2019.

Guevara, M., Jorba, O., Tena, C., Denier van der Gon, H., Kuenen, J., Elguindi, N., Darras, S., Granier, C., and Pérez García-Pando, C.: Copernicus Atmosphere Monitoring Service TEMPOral profiles (CAMS-TEMPO): global and European emission temporal profile maps for atmospheric chemistry modelling, Earth Syst. Sci. Data, 13, 367–404, https://doi.org/10.5194/essd-13-367-2021, 2021.

Hersbach, H., Bell, B., Berrisford, P., Hirahara, S., Horányi, A., Muñoz-Sabater, J., Nicolas, J., Peubey, C., Radu, R., Schepers, D., Simmons, A., Soci, C., Abdalla, S., Abellan, X., Balsamo, G., Bechtold, P., Biavati, G., Bidlot, J., Bonavita, M., De Chiara, G., Dahlgren, P., Dee, D., Diamantakis, M., Dragani, R., Flem ming, J., Forbes, R., Fuentes, M., Geer, A., Haimberger, L., Healy, S., Hogan, R. J., Hólm, E., Janisková, M., Keeley, S., Laloyaux, P., Lopez, P., Lupu, C., Radnoti, G., de Rosnay, P., Rozum, I., Vamborg, F., Villaume, S., and Thépaut, J.-N.: The ERA5 global reanalysis, Q. J. Roy. Meteor. Soc., 146, 19992049, https://doi.org/10.1002/qj.3803, 2020.

Ho, D., Gałkowski, M., Reum, F., Botía, S., Marshall, J., Totsche, K. U., and Gerbig, C.: Recommended coupling to global meteorological fields for long-term tracer simulations with WRF-GHG, Geosci. Model Dev., 17, 7401–7422, https://doi.org/10.5194/gmd-17-7401-2024, 2024.

670   Hong, S.-Y., Noh, Y., and Dudhia, J.: A New Vertical Diffusion Package with an Explicit Treatment of Entrainment Processes, Mon. Weather Rev., 134, 2318–2341, https://doi.org/10.1175/MWR3199.1, 2006.

Hu, X.-M., Gourdji, S. M., Davis, K. J., Wang, Q., Zhang, Y., Xue, M., Feng, S., Moore, B., and Crowell, S. M.: Implementation of improved parameterization of terrestrial flux in WRF-VPRM improves the simulation of nighttime CO_2 peaks and a daytime CO_2 band ahead of a cold front, J. Geophys. Res.-Atmos., 126, e2020JD034362,

675   https://doi.org/10.1029/2020JD034362, 2021.

Huete, A., Didan, K., Miura, T., Rodriguez, E., Gao, X., and Ferreira, L.: Overview of the radiometric and biophysical performance of the MODIS vegetation indices, Remote Sens. Environ., 83, 195–213, https://doi.org/10.1016/S0034-4257(02)00096-2, 2002.

ICOS RI, Apadula, F., Arnold, S., Bergamaschi, P., Biermann, T., Chen, H., Colomb, A., Conil, S., Couret, C., Cristofanelli,

680   P., De Mazière, M., Delmotte, M., Emmenegger, L., Forster, G., Frumau, A., Hatakka, J., Heliasz, M., Heltai, D., Hensen, A., Hermansen, O., Hoheisel, A., Kneuer, T., Komínková, K., Kubistin, D., Laurent, O., Laurila, T., Lehner, I., Lehtinen, K., Leskinen, A., Leuenberger, M., Levula, J., Lindauer, M., Lopez, M., Lund Myhre, C., Lunder, C., Mammarella, I., Manca, G., Manning, A., Marek, M., Marklund, P., Meinhardt, F., Mölder, M., Müller-Williams, J., O'Doherty, S., Ottosson-Löfvenius, M., Piacentino, S., Pichon, J.-M., Pitt, J., Platt, S.M., Plaß-Dülmer, C., Ramonet, M., Rivas-Soriano, P., Roulet, Y.-A.,

685   Scheeren, B., Schmidt, M., Schumacher, M., Sha, M.K., Smith, P., Stanley, K., Steinbacher, M., Sørensen, L.L., Trisolino, P., Vítková, G., Yver-Kwok, C., di Sarra, A.. ICOS Atmosphere Release 2023-1 of Level 2 Greenhouse Gas Mole Fractions of CO_2, CH_4, N_2O, CO, meteorology and $^{14}CO_2$, and flask samples analysed for CO_2, CH_4, N_2O, CO, H_2 and SF_6. https://doi.org/10.18160/VXCS-95EV, 2023

Inness, A., Ades, M., Agustí-Panareda, A., Barré, J., Benedictow, A., Blechschmidt, A.-M., Dominguez, J. J., Engelen, R.,

690   Eskes, H., Flemming, J., Huijnen, V., Jones, L., Kipling, Z., Massart, S., Parrington, M., Peuch, V.-H., Razinger, M., Remy, S., Schulz, M., and Suttie, M.: The CAMS reanalysis of atmospheric composition, Atmos. Chem. Phys., 19, 3515–3556, https://doi.org/10.5194/acp-19-3515-2019, 2019.Junkermann, W., Hagemann, R., and Vogel, B.: Nucleation in the Karlsruhe plume during the COPS/TRACKS-Lagrange experiment, Q. J. Royal Meteor. Soc., 137, 267–274, 2011

Karbasi, S., Abdi, A.H., Malakooti, H., and Orza, J.A.G.: Atmospheric CO_2 column concentration over Iran: emissions,

695   GOSAT satellite observations, and WRF-GHG model simulations, Atmos. Res., 314, https://doi.org/10.1016/j.atmosres.2024.107818, 2025.

Karbasi, S.; Malakooti, H.; Rahnama, M.; Azadi, M.: Study of mid-latitude retrieval XCO_2 greenhouse gas: Validation of satellite-based shortwave infrared spectroscopy with ground-based TCCON observations, Sci. Total Environ. 836, https://doi.org/10.1016/j.scitotenv.2022.155513, 2022.

700 Kuenen, J., Dellaert, S., Visschedijk, A., Jalkanen, J.-P., Super, I., and Denier van der Gon, H.: CAMS-REG-v4: a state-of-the-art high-resolution European emission inventory for air quality modelling, Earth Syst. Sci. Data, 14, 491–515, https://doi.org/10.5194/essd-14-491-2022, 2022.

Kusaka, H., Kondo, H., Kikegawa, Y., and Kimura, F.: A simple single-layer urban canopy model for atmospheric models: comparison with multi-layer and slab models, Boundary-Layer Meteorol. 101, 329–358. https://doi.org/10.1023/
705 A:1019207923078, 2001.

Lan, X., Tans, P. P., and Thoning, K.W.: Trends in globally-averaged CO_2 determined from NOAA Global Monitoring Laboratory measurements (last access: 05 June 2025), https://doi.org/10.15138/9N0H-ZH07, 2025.

Landschützer, P., Bushinsky, S., Gray, A. R.: A combined globally mapped CO_2 flux estimate based on the Surface Ocean CO_2 Atlas Database (SOCAT) and Southern Ocean Carbon and Climate Observations and Modeling (SOCCOM)
710 biogeochemistry floats from 1982 to 2017 (NCEI Accession 0191304). Version 2.2. NOAA National Centers for Environmental Information (last access: 05 June 2025), https://doi.org/10.25921/9hsn-xq82, 2019.

Laughner, J. L., Toon, G. C., Mendonca, J., Petri, C., Roche, S., Wunch, D., Blavier, J.-F., Griffith, D. W. T., Heikkinen, P., Keeling, R. F., Kiel, M., Kivi, R., Roehl, C. M., Stephens, B. B., Baier, B. C., Chen, H., Choi, Y., Deutscher, N. M., DiGangi, J. P., Gross, J., Herkommer, B., Jeseck, P., Laemmel, T., Lan, X., McGee, E., McKain, K., Miller, J., Morino, I., Notholt, J.,
715 Ohyama, H., Pollard, D. F., Rettinger, M., Riris, H., Rousogenous, C., Sha, M. K., Shiomi, K., Strong, K., Sussmann, R., Té, Y., Velazco, V. A., Wofsy, S. C., Zhou, M., and Wennberg, P. O.: The Total Carbon Column Observing Network's GGG2020 data version, Earth Syst. Sci. Data, 16, 2197–2260, https://doi.org/10.5194/essd-16-2197-2024, 2024.

Lian, J., Bréon, F.-M., Broquet, G., Lauvaux, T., Zheng, B., Ramonet, M., Xueref-Remy, I., Kotthaus, S., Haeffelin, M., and Ciais, P.: Sensitivity to the sources of uncertainties in the modeling of atmospheric CO_2 concentration within and in the vicinity
720 of Paris, Atmos. Chem. Phys., 21, 10707–10726, https://doi.org/10.5194/acp-21-10707-2021, 2021.

Lin, J. C., Gerbig, C., Wofsy, S. C., Andrews, A. E., Daube, B. C., Davis, K. J., and Grainger, C. A.: A near-field tool for simulating the upstream influence of atmospheric observations: The Stochastic Time-Inverted Lagrangian Transport (STILT) model, J. Geophys. Res., 108, 4493, https://doi.org/10.1029/2002JD003161, 2003.

Liu, X., Cao, J., and Xin, D.: Wind field numerical simulation in forested regions of complex terrain: A mesoscale study using
725 WRF, J. Wind Eng. Ind. Aerodyn. 222, 10491, https://doi.org/10.1016/j.jweia.2022.104915, 2022.

Mahadevan, P., Wofsy, S. C., Matross, D. M., Xiao, X., Dunn, A. L., Lin, J. C., Gerbig, C., Munger, J. W., Chow, V. Y., and Gottlieb, E. W.: A satellite-based biosphere parameterization for net ecosystem CO_2 exchange: Vegetation Photosynthesis and Respiration Model (VPRM), Global Biogeochem. Cy., 22, GB2005, https://doi.org/10.1029/2006GB002735, 2008.

Maksyutov, S., Eggleston, S., Woo, J. H., Fang, S., Witi, J., Gillenwater, M., Goodwin, J., and Tubiello, F.: 2019 Refinement
730 to the 2006 IPCC Guidelines for National Greenhouse Gas Inventories, Vol. 1, IPCC, Switzerland, https://www.ipcc-nggip.iges.or.jp/public/2019rf/index.html (last access: 12 February 2025), 2019.

Mar, K. A., Ojha, N., Pozzer, A., and Butler, T. M.: Ozone air quality simulations with WRF-Chem (v3.5.1) over Europe: model evaluation and chemical mechanism comparison, Geosci. Model Dev., 9, 3699–3728, https://doi.org/10.5194/gmd-9-3699-2016, 2016.

735   Martilli, A., Clappier, A., Rotach, and M.W.: An urban surface exchange parameterisation for mesoscale models, Bound.-Layer Meteor., 104, 261–304. https:// doi.org/10.1023/A:1016099921195, 2002.

Nassar, R., Napier-Linton, L., Gurney, K. R., Andres, R. J., Oda, T., Vogel, F. R., and Deng, F.: Improving the temporal and spatial distribution of CO_2 emissions from global fossil fuel emission data sets, J. Geophys. Res.-Atmos., 118, 917–933, https://doi.org/10.1029/2012JD018196, 2013.

740   Ngan, F., H. Kim, P. Lee, K. Al-Wali, and B. Dornblaser.: A study of nocturnal surface wind speed overprediction by the WRF-ARW model in southeastern Texas, J. Appl. Meteor. Climatol., 52, 2638–2653, https://doi.org/10.1175/JAMC-D-13-060.1, 2013.

Ostler, A., Sussmann, R., Patra, P. K., Houweling, S., De Bruine, M., Stiller, G. P., Haenel, F. J., Plieninger, J., Bousquet, P., Yin, Y., Saunois, M., Walker, K. A., Deutscher, N. M., Griffith, D. W. T., Blumenstock, T., Hase, F., Warneke, T., Wang, Z.,

745   Kivi, R., and Robinson, J.: Evaluation of column-averaged methane in models and TCCON with a focus on the stratosphere, Atmos. Meas. Tech., 9, 4843–4859, https://doi.org/10.5194/amt-9-4843-2016, 2016.

Pillai, D., Gerbig, C., Ahmadov, R., Rödenbeck, C., Kretschmer, R., Koch, T., Thompson, R., Neininger, B., and Lavrié, J. V.: High-resolution simulations of atmospheric CO_2 over complex terrain – representing the Ochsenkopf mountain tall tower, Atmos. Chem. Phys., 11, 7445–7464, https://doi.org/10.5194/acp-11-7445-2011, 2011.

750   Poraicu, C., Müller, J.-F., Stavrakou, T., Fonteyn, D., Tack, F., Deutsch, F., Laffineur, Q., Van Malderen, R., and Veldeman, N.: Cross-evaluating WRF-Chem v4.1.2, TROPOMI, APEX, and in situ NO_2 measurements over Antwerp, Belgium, Geosci. Model Dev., 16, 479–508, https://doi.org/10.5194/gmd-16-479-2023, 2023.

Pörtner, H.-O., Roberts, D., Tignor, M., Poloczanska, E., Mintenbeck, K., Alegría, A., Craig, M., Langsdorf, S., Löschke, S., Möller, V., Okem, A., Rama, B., and Ayanlade, S.: Climate Change 2022: Impacts, Adaptation and Vulnerability Working

755   Group II Contribution to the Sixth Assessment Report of the Intergovernmental Panel on Climate Change, Cambridge University Press, https://doi.org/10.1017/9781009325844, 2022.

Ramonet, M., Ciais, P., Apadula, F., Bartyzel, J., Bastos, A., Bergamaschi, P., Blanc, P. E., Brunner, D., Caracciolo di Torchiarolo, L., Calzolari, F., Chen, H., Chmura, L., Colomb, A., Conil, S., Cristofanelli, P., Cuevas, E., Curcoll, R., Delmotte, M., di Sarra, A., Emmenegger, L., Forster, G., Frumau, A., Gerbig, C., Gheusi, F., Hammer, S., Haszpra, L., Hatakka, J.,

760   Hazan, L., Heliasz, M., Henne, S., Hensen, A., Hermansen, O., Keronen, P., Kivi, R., Komínková, K., Kubistin, D., Laurent, O., Laurila, T., Lavric, J. V., Lehner, I., Lehtinen, K. E. J., Leskinen, A., Leuenberger, M., Levin, I., Lindauer, M., Lopez, M., Myhre, C. L., Mammarella, I., Manca, G., Manning, A., Marek, M. V., Marklund, P., Martin, D., Meinhardt, F., Mihalopoulos, N., Mölder, M., Morgui, J. A., Necki, J., O'Doherty, S., O'Dowd, C., Ottosson, M., Philippon, C., Piacentino, S., Pichon, J. M., Plass-Duelmer, C., Resovsky, A., Rivier, L., Rodó, X., Sha, M. K., Scheeren, H. A., Sferlazzo, D., Spain, T. G., Stanley, K. M.,

765   Steinbacher, M., Trisolino, P., Vermeulen, A., Vítková, G., Weyrauch, D., Xueref-Remy, I., Yala, K., and Yver Kwok, C.:

The fingerprint of the summer 2018 drought in Europe on ground-based atmospheric CO_2 measurements, Philos. T. Roy. Soc. B, 375, 20190513, https://doi.org/10.1098/rstb.2019.0513, 2020.

Rodgers, C. D., and Connor, B. J.: Intercomparison of remote sounding instruments, J. Geophys. Res.-Atmos., 108, 4116, https://doi.org/10.1029/2002JD002299, 2003.

770 Saito, R., Patra, P. K., Deutscher, N., Wunch, D., Ishijima, K., Sherlock, V., Blumenstock, T., Dohe, S., Griffith, D., Hase, F., Heikkinen, P., Kyrö, E., Macatangay, R., Mendonca, J., Messerschmidt, J., Morino, I., Notholt, J., Rettinger, M., Strong, K., Sussmann, R., and Warneke, T.: Technical Note: Latitude-time variations of atmospheric column-average dry air mole fractions of CO_2, CH_4 and N_2O, Atmos. Chem. Phys., 12, 7767–7777, https://doi.org/10.5194/acp-12-7767-2012, 2012.

Sánchez-Benítez, A., Goessling, H., Pithan, F., Semmler, T., and Jung, T.: The July 2019 European Heat Wave in a Warmer

775 Climate: Storyline Scenarios with a Coupled Model Using Spectral Nudging, J. Climate, 35, 2373–2390, https://doi.org/10.1175/JCLI-D-21-0573.1, 2022.

Smith, N. E., Kooijmans, L. M., Koren, G., van Schaik, E., van der Woude, A. M., Wanders, N., Ramonet, M., Xueref-Remy, I., Siebicke, L., Manca, G., Brümmer, C., Baker, I. T., Haynes, K. D., Luijkx, I., and Peters, W.: Spring enhancement and summer reduction in carbon uptake during the 2018 drought in northwestern Europe, Philos. T. R. Soc. B, 375, 20190509,

780 https://doi.org/10.1098/rstb.2019.0509, 2020.

Sousa, P. M., D. Barriopedro, R. García-Herrera, C. Ordóñez, P. M. M. Soares, and R. M. Trigo.: Distinct influences of large-scale circulation and regional feedbacks in two exceptional 2019 European heatwaves, Commun. Earth Environ., 1, 48, https://doi.org/10.1038/s43247-020-00048-9, 2020.

Storm, I., Karstens, U., D'Onofrio, C., Vermeulen, A., and Peters, W.: A view of the European carbon flux landscape through

785 the lens of the ICOS atmospheric observation network, Atmos. Chem. Phys., 23, 4993–5008, https://doi.org/10.5194/acp-23-4993-2023, 2023.

Super, I., Dellaert, S. N. C., Visschedijk, A. J. H., and Denier van der Gon, H. A. C.: Uncertainty analysis of a European high-resolution emission inventory of CO_2 and CO to support inverse modelling and network design, Atmos. Chem. Phys., 20, 1795–1816, https://doi.org/10.5194/acp-20-1795-2020, 2020.

790 Thilakan, V., Pillai, D., Sukumaran, J., Gerbig, C., Hakkim, H., Sinha, V., Terao, Y., Naja, M., and Deshpande, M. V.: Potential of using CO_2 observations over India in a regional carbon budget estimation by improving the modelling system, Atmos. Chem. Phys., 24, 5315–5335, https://doi.org/10.5194/acp-24-5315-2024, 2024.

Thompson, R. L., Broquet, G., Gerbig, C., Koch, T., Lang, M., Monteil, G., Munassar, S., Nickless, A., Scholze, M., Ramonet, M., Karstens, U., van Schaik, E., Wu, Z., and Rödenbeck, C.: Changes in net ecosystem exchange over Europe during the

795 2018 drought based on atmospheric observations, Philos. T. Roy. Soc. B, 375, 20190512, https://doi.org/10.1098/rstb.2019.0512, 2020.

Tuccella, P., Curci, G., Visconti, G., Bessagnet, B., Menut, L., and Park, R. J.: Modeling of gas and aerosol with WRF/Chem over Europe: evaluation and sensitivity study, J. Geophys. Res., 117, D03303, https://doi.org/10.1029/2011JD016302, 2012.

Turner, A. J., Jacob, D. J., Wecht, K. J., Maasakkers, J. D., Lundgren, E., Andrews, A. E., Biraud, S. C., Boesch, H., Bowman, K. W., Deutscher, N. M., Dubey, M. K., Griffith, D. W. T., Hase, F., Kuze, A., Notholt, J., Ohyama, H., Parker, R., Payne, V. H., Sussmann, R., Sweeney, C., Velazco, V. A., Warneke, T., Wennberg, P. O., and Wunch, D.: Estimating global and North American methane emissions with high spatial resolution using GOSAT satellite data, Atmos. Chem. Phys., 15, 7049–7069, https://doi.org/10.5194/acp-15-7049-2015, 2015.

van der Woude, A. M., de Kok, R., Smith, N., Luijkx, I. T., Botía, S., Karstens, U., Kooijmans, L. M. J., Koren, G., Meijer, H. A. J., Steeneveld, G.-J., Storm, I., Super, I., Scheeren, H. A., Vermeulen, A., and Peters, W.: Near-real-time CO_2 fluxes from CarbonTracker Europe for high-resolution atmospheric modeling, Earth Syst. Sci. Data, 15, 579–605, https://doi.org/10.5194/essd-15-579-2023, 2023.

Velazco, V. A., Deutscher, N. M., Morino, I., Uchino, O., Bukosa, B., Ajiro, M., Kamei, A., Jones, N. B., Paton-Walsh, C., and Griffith, D. W. T.: Satellite and ground-based measurements of XCO_2 in a remote semiarid region of Australia, Earth Syst. Sci. Data. 11, 935–946. https://doi.org/10.5194/essd-11-935-2019, 2019.

Wiedinmyer, C., Kimura, Y., McDonald-Buller, E. C., Emmons, L. K., Buchholz, R. R., Tang, W., Seto, K., Joseph, M. B., Barsanti, K. C., Carlton, A. G., and Yokelson, R.: The Fire Inventory from NCAR version 2.5: an updated global fire emissions model for climate and chemistry applications, Geosci. Model Dev., 16, 3873–3891, https://doi.org/10.5194/gmd-16-3873-2023, 2023.

Wu, L., Hasekamp, O., Hu, H., Landgraf, J., Butz, A., aan de Brugh, J., Aben, I., Pollard, D. F., Griffith, D. W. T., Feist, D. G., Koshelev, D., Hase, F., Toon, G. C., Ohyama, H., Morino, I., Notholt, J., Shiomi, K., Iraci, L., Schneider, M., De Mazière, M., Sussmann, R., Kivi, R., Warneke, T., Goo, T.-Y., and Té, Y.: Carbon dioxide retrieval from OCO-2 satellite observations using the RemoTeC algorithm and validation with TCCON measurements, Atmos. Meas. Tech., 11, 3111–3130, https://doi.org/10.5194/amt-11-3111-2018, 2018.

Wunch, D., Toon, G. C., Blavier, J.-F. L., Washenfelder, R. A., Notholt, J., Connor, B. J., Griffith, D. W. T., Sherlock, V., and Wennberg, P. O.: The Total Carbon Column Observing Network, Philos. T. Roy. Soc. A, 369, 2087–2112, https://doi.org/10.1098/rsta.2010.0240, 2011.

Xiao, X., D. Hollinger, J. Aber, M. Goltz, E. A. Davidson, Q. Zhang, and B. Moore III.: Satellite-based modeling of gross primary production in an evergreen needleleaf forest, Remote Sens. Environ., 89, 519-534, https://doi.org/10.1016/j.rse.2003.11.008, 2004.

Yang, D., Boesch, H., Liu, Y., Somkuti, P., Cai, Z., Chen, X., Di, Noia. A., Lin, C., Lu, N., Lyu, D., Parker, R. J., Tian, L., Wang, M., Webb, A., Yao, L., Yin, Z., Zheng, Y., Deutscher, N. M., Griffith, D. W. T., Hase, F., Kivi, R., Morino, I., Notholt, J., Ohyama, H., Pollard, D. F., Shiomi, K., Sussmann, R., Té, Y., Velazco, V. A., Warneke, T., and Wunch, D.: Toward high precision XCO_2 retrievals from TanSat observations: retrieval improvement and validation against TCCON measurements. J Geophys Res. 125. https://doi.org/10.1029/2020JD032794, 2020.

Yang, H., Wu, K., Wang, T., Wang, P., and Zhou, M.: Atmospheric anthropogenic CO_2 variations observed by tower in-situ measurements and simulated by the STILT model in the Beijing megacity region, Atmos. Res., 325, 108258, 0169-8095, https://doi.org/10.1016/j.atmosres.2025.108258, 2025.

Yarragunta, Y., Francis, D., Fonseca, R., and Nelli, N.: Evaluation of the WRF-Chem performance for the air pollutants over the United Arab Emirates, Atmos. Chem. Phys., 25, 1685–1709, https://doi.org/10.5194/acp-25-1685-2025, 2025.

Zhang, D., and Zheng, W.: Diurnal Cycles of Surface Winds and Temperatures as Simulated by Five Boundary Layer Parameterizations, J. Appl. Meteorol., 43, 157–169, https://doi.org/10.1175/1520-0450(2004)043<0157:DCOSWA>2.0.CO;2, 2004.

Zhao, X., Chen, J., Marshall, J., Gałkowski, M., Hachinger, S., Dietrich, F., Shekhar, A., Gensheimer, J., Wenzel, A., and Gerbig, C.: Understanding greenhouse gas (GHG) column concentrations in Munich using the Weather Research and Forecasting (WRF) model, Atmos. Chem. Phys., 23, 14325–14347, https://doi.org/10.5194/acp-23-14325-2023, 2023.

Zhao, X., Marshall, J., Hachinger, S., Gerbig, C., Frey, M., Hase, F., and Chen, J.: Analysis of total column CO_2 and CH4 measurements in Berlin with WRF-GHG, Atmos. Chem. Phys., 19, 11279–11302, https://doi.org/10.5194/acp-19-11279-2019, 2019.

Zhou, M., Dils, B., Wang, P., Detmers, R., Yoshida, Y., O'Dell, C. W., Feist, D. G., Velazco, V. A., Schneider, M., and De Mazière, M.: Validation of TANSO-FTS/GOSAT XCO_2 and XCH_4 glint mode retrievals using TCCON data from near-ocean sites, Atmos. Meas. Tech., 9, 1415–1430, https://doi.org/10.5194/amt-9-1415-2016, 2016.

Zhou, M., Ni, Q., Cai, Z., Langerock, B., Nan, W., Yang, Y., Che, K., Yang, D., Wang, T., Liu, Y., and Wang, P.: CO_2 in Beijing and Xianghe Observed by Ground-Based FTIR Column Measurements and Validation to OCO-2/3 Satellite Observations, Remote Sens., 14, 3769. https://doi.org/10.3390/rs14153769, 2022.